Role of thermodynamic and turbulence processes on the fog life cycle during SOFOG3D experiment

Cheikh DIONE[1*], Martial HAEFFELIN[1], Frederic BURNET[2], Christine LAC[2], Guylaine CANUT[2], Julien DELANOË[3], Jean-Charles DUPONT[4], Susana JORQUERA[3], Pauline MARTINET[2], Jean-Francois RIBAUD[5], and Felipe TOLEDO[3]

1) Institut Pierre Simon Laplace, CNRS, École Polytechnique, Institut Polytechnique de Paris, Paris, France

2) CNRM, Université de Toulouse, Météo-France, CNRS, Toulouse, France

3) Laboratoire Atmosphères, Milieux, Observations Spatiales/UVSQ/CNRS/UPMC, 78280 Guyancourt, France

4) Institut Pierre-Simon Laplace, École Polytechnique, UVSQ, Université Paris-Saclay, 91128 Palaiseau, France

5) Laboratoire de Météorologie Dynamique, École Polytechnique, Institut Polytechnique de Paris, 91128 Palaiseau, France.

* corresponding author: Cheikh DIONE, cdione@ipsl.fr

Abstract:

In this study, we use a synergy of in-situ and remote sensing measurements collected during the SOuthwest FOGs 3D experiment for processes study (SOFOG3D) field campaign in autumn and winter 2019-2020, to analyze the thermodynamic and turbulent processes related to fog formation, evolution, and dissipation across southwestern France. Based on a unique measurement dataset (synergy of cloud radar, microwave radiometer, wind lidar, and weather station) combined with a fog conceptual model, an analysis of the four deepest fog episodes (two radiation fogs and two advection-radiation fogs) is conducted. The results show that radiation and advection-radiation fogs form under deep and thin temperature inversions, respectively. For both fog categories, the transition period from stable to adiabatic fog and the fog adiabatic phase are driven by vertical mixing associated with an increase in turbulence in the fog layer due to mechanical production (turbulence kinetic energy (TKE) up to 0.4 $m^2\,s^{-2}$ and vertical velocity variance (σ_w^2) up to 0.04 $m^2\,s^{-2}$) generated by increasing wind and wind shear . Our study reveals that fog liquid water path, fog top height, temperature and radar reflectivity profiles and fog adiabaticity derived from the conceptual model evolve in a consistent manner to clearly characterize this transition. The dissipation time is observed at night for the advection-radiation fog case studies and after sunrise for the radiation fog case studies. Night-time dissipation is driven by horizontal advection generating mechanical turbulence (TKE at least 0.3 $m^2\,s^{-2}$ and σ_w^2 larger than 0.04 $m^2\,s^{-2}$). Daytime dissipation is linked to the combination of thermal and mechanical turbulence related respectively to solar heating (near surface sensible heat flux larger than 10 $W\,m^{-2}$) and wind shear. This study demonstrates the added value of monitoring fog liquid water content and depth, combined with wind, turbulence and temperature profiles, and diagnostics such as fog liquid water reservoir and adiabaticity to better explain the drivers of the fog life cycle.

Key words: Fog conceptual model, radiation/advection fog, fog life cycle, turbulence, Southwestern France, SOFOG3D

1. Introduction

Fog is an extreme meteorological phenomenon forming in several regions of earth under different atmospheric conditions depending on the season and location (Gultepe et al., 2007). It is defined by the suspension of water droplets in the lowest troposphere which reduces the horizontal visibility to lower or at least 1000 m. Fog has significant negative impacts on air, road and marine traffic causing large economical and human losses (Bartok et al., 2012, Bartoková et al., 2015, Huang and Chen, 2016). It also has a high impact on solar energy, particularly in the mid-latitudes during autumn and winter. Based on in-situ measurements, several studies have focused on fog formation at different regions and highlighted the main processes leading to its initiation allowing to define five categories of fog: radiation fog (Price 2019), advection-radiation fog (Gultepe et al., 2007, 2009; Niu et al., 2010a, b, Dupont et al., 2012), advection fog (Koračin et al., 2014; Liu et al., 2016, Fernando et al., 2021), fog by stratus lowering (Koračin et al., 2011; Fathalli et al., 2022) and precipitation fog (Tardif and Rasmussen, 2007; Liu et al., 2012). According to the literature, several processes are identified to drive fog evolution and dissipation depending on each category. Fog formation requires low intensity of turbulence (Nakanishi 2000; Bergot 2013; Price 2019).

Dhangar et al., 2021 found that optically thin fog develops under low-turbulence kinetic energy and the transition to dense fog is observed when the turbulence increases and reaches enough values to allow the vertical mixing of the fog layer. The dissipation of radiation fog is usually observed after sunrise and linked with the increase in solar heating leading to the evaporation of water drops and a vertical mixing of water vapor (Roach, 1995; Haeffelin et al., 2010; Maalick et al., 2016). Bergot et al., 2015 relied on large eddy simulations (LES) to characterize the role of dry downdrafts in allowing solar radiation to reach the ground and increase the turbulence, leading to the dissipation. Additionally, Pauli et al., 2022 studied the climatology of fog and low stratus cloud formation and dissipation times in Central Europe using satellite data and showed that fog dissipation is also often related to topography. The dissipation processes are more difficult to study then the fog formation processes, due to the complexity of fog's scale. At the state of the art, based on case studies, numerical weather prediction models (Philip et al., 2016, Bell et al., 2022) and high resolution models (Price et al., 2018, Ducongé et al., 2020, Fathalli et al., 2022) up to LES (Bergot et al., 2015, Mazoyer et al., 2017) have the ability to simulate fog formation in several complex areas. However, they have difficulties in simulating the processes driving fog evolution over land in real time (Steeneveld *et al.*, 2015, Price et al., 2015, Román-Cascón et al., 2016; Wærsted et al., 2019; Pithani et al., 2020, Boutle *et al.*, 2022).

67   Toledo et al., 2021 developed a one-column conceptual model of adiabatic continental fog
68 allowing to define key fog metrics as the equivalent fog adiabaticity by closure and the reservoir of
69 liquid water path (RLWP) that can be estimated in real-time and allowing a diagnostic of fog
70 evolution. Based on seven years of measurements collected at SIRTA (Site Instrumental de
71 Recherche par Télédétection Atmosphérique), a French observatory located at Palaiseau/France,
72 Toledo et al., 2021 have validated their model on the timing of fog dissipation using the RLWP.
73 The limitation of this model is that the estimation of the reservoir depends on fog specific
74 parameters and does not take into account local (turbulence) or large scale (advection) processes .
75 Indeed, to further understand uncertainties associated with the estimation of the RLWP, the
76 validation of the model using data from other measurement sites having a large occurrence of fog is
77 another step before using it as a nowcasting tool.

78   Finding the right instruments allowing nowcasting fog is also another challenge that can be
79 partly resolved by field campaigns combining both in-situ and remote sensing measurements and
80 numerical simulations. At the state of the art, nowcasting fog requires more efforts in in-situ
81 measurements and modelling. In this context, the SOuth westFOGs 3D (SOFOG3D) project, led by
82 Météo-France, was designed to document local processes involved in fog formation, evolution and
83 dissipation to better improve its predictability in numerical weather prediction models.

84   In order to improve our understanding of the processes driving the fog life cycle and to
85 validate the fog conceptual model from Toledo et al., 2021 on another region than the one on which
86 it has been developed, the current study aims at identifying the main dynamical and thermodynamic
87 processes driving fog's formation, evolution, and dissipation in the framework of SOFOG3D
88 project. In particular, the role of horizontal advection, atmospheric stability and turbulence is further
89 analyzed to better identify the drivers of radiation and radiation-advection fog phases. Using an
90 instrumental synergy of in-situ and remote sensing measurements and the fog conceptual model, the
91 phenomenology of fog and the different phases driving its evolution are deeply analyzed
92 considering four heavy fog case studies observed over Southwestern France during Winter 2019-
93 2020.

94   This paper is structured into five sections. The datasets and methodological approach are
95 described in the following section. Section 3 gives an analysis of the processes involved in fog
96 evolution based on two different categories of fog formation phenomenology. Section 4 includes a
97 discussion on the thermodynamical and turbulent processes driving the fog phases and Section 5
98 presents the conclusion.

99 **2. Data and methodology**

In a mesoscale context, the SOFOG3D field experiment is located in Southwestern France, in the Nouvelle Aquitaine region (Fig. 1a). The field campaign was carried out during the autumn and winter 2019-2020 period leading to 15 intensive observation periods (IOPs). A unique dataset has been collected across a complex region with a very contrasted topography. This region is bordered in the east by the "Massif Central", in the west by the Atlantic Ocean, in the north by Bordeaux and in the south by the "Pyrenees". In the region, several dynamical effects can be observed such as sea breeze, land breeze, and mesoscale foehn circulations influencing the fog life cycle. At the local scale, the supersite under focused here is bordered by two rivers: "La Garonne" to the East and "L'Eyre" to the west (Fig. 1a). These two rivers and the surrounding surface heterogeneities can modulate the fog formation and dissipation times. During the campaign, several in-situ and remote sensing measurements were jointly deployed in the studied area of SOFOG3D. In this paper, our analysis focuses on the data collected in the surroundings of the supersite at Charbonnière, the most instrumented site (Fig. 1b). Below, the descriptions of the in-situ and remote sensing measurements and then the fog conceptual model are presented with emphasis on the main meteorological variables used in this study.

2.1 Dataset

2.1.1 Surface measurement data

A network of surface weather stations was installed in the study domain of SOFOG3D at the vicinity of Charbonnière, to document the spatial variability of fog and surface heterogeneities at the local scale (Fig. 1b). Four weather stations were also deployed around the supersite in a northeast-southwest transect (Fig. 1b). These stations were installed at Moustey, Cape Sud, Tuzan and Noaillan, almost at the same altitude, and operated continuously with very high temporal resolution (0.1 s time interval) during the period from 18 October 2019 to 31 December 2020. In addition to temperature, pressure, relative humidity sensors and anemometer, a scatterometer provided the visibility used to estimate fog formation and dissipation times at each station. Temperature data are used to characterize the spatial variability of the radiative cooling, and wind speed and direction the local circulations.

In this study, fog occurrence is defined using the visibility at the supersite based on an algorithm developed by Tardif and Rasmussen, 2007. This algorithm consists of dividing visibility time series into 10 min blocks. A fog block means that half of the visibility measurements during a 10 min period are below 1000 m. Blocks are characterized by a positive or negative construct. A positive construct indicates that five consecutive blocks of which the central block is fog and at least two other blocks are also fog blocks. The opposite means a negative construct. Thus, the fog

133 formation time corresponds to the first fog block in the first positive construct encountered. The fog
134 dissipation time corresponds to the last fog block in the last positive construct before either a
135 negative construct or three consecutive non-fog blocks are encountered. This algorithm discards fog
136 events shorter than 1 hour.

137 Meteo-France installed in a fallow field near the supersite, several sensors as Licor analyzers
138 and sonic anemometers to continuously measure the near-surface (3 m a.g.l) meteorological
139 conditions (air temperature and relative humidity), the three components of the wind, and pressure
140 at 0.3 m a.g.l). These instruments provided high frequency data at 20 Hz. In this study, to document
141 turbulence and thermodynamical processes driving fog phases, we use the sensible heat flux (SHF),
142 turbulence kinetic energy (TKE), and vertical velocity variance (σ_w^2). These variables are estimated
143 using the Eddy-covariance methods (Foken et al., 2004, Mauder et al., 2013) calculated every 30
144 minutes after a high quality control of the data. More details on the data can be found in Canut,
145 2020.

2.1.2 Observation of cloud characteristics

147 For the monitoring of cloud layers, a BASTA cloud radar (Delanoë et al., 2016) was
148 deployed at Charbonnière and a CL51 Ceilometer at Tuzan (7.4 km northwest of Charbonnière)
149 (Fig. 1b).

150 BASTA is a 95-GHz cloud radar manufactured by the Laboratoire Atmosphères, Milieux,
151 Observations Spatiales (LATMOS) with an absolute calibration method for frequency-modulated
152 continuous wave (FMCW) cloud radars based on corner reflectors (Toledo et al., 2020). From 7
153 November 2019 to 12 March 2020, the radar was operated continuously with a vertical pointing
154 mode having three vertical resolutions (12.5 m, 25 m, and 100 m). It provided radar reflectivity and
155 Doppler velocity. The lowest mode, having its first available gate at 37.5 m a.g.l and 12.5 m of
156 vertical resolution, is used to estimate the cloud top height (CTH) which gives the fog thickness at a
157 time resolution of 30 seconds. It also provides the level of highest concentration of droplets in the
158 fog layer. The CTH is estimated using a radar reflectivity threshold of -34 dBZ.

159 The CL51 is manufactured by Vaisala and automatically provided three estimates of cloud
160 base height (CBH) allowing the detection of cloud decks every 30 seconds with a vertical resolution
161 of 15 m from 10 October 2019 to 2 April 2020. In this study, we use the lowest CBH, which
162 corresponds to the base height of stratus cloud lowering or lifting when fog forms or dissipates,
163 respectively. More information on the data provided by the CL51 can be found in Burnet, 2021.

2.1.3 Temperature, liquid water content, and wind profiling

A microwave radiometer Hatpro (MWR) manufactured by Radiometer Physics GmbH (RPG) was installed at the supersite to characterize thermodynamic atmospheric conditions during the field campaign. From 4 December 2019 to 9 May 2020, the MWR operated continuously at the supersite using two spectral-bands: the K-band which 22.24-31 GHz used for the retrieval of humidity profiles, integrated water vapor (IWV) content and liquid water path (LWP), and the V-band which 51-58 GHz to retrieve temperature profiles. In order to improve the vertical resolution in the boundary layer, the MWR was set up to scan in 10 elevation angles (5° above ground level) every 10 minutes with a zenith pointing each 1 second. Using neural networks, brightness temperatures measured by the MWR at all elevation angles (the lower elevations angles added to measurements at zenith) are inverted to temperature and humidity variables. More details on this method can be found in Martinet et al., 2022. Comparing temperature and humidity profiles retrieved by the MWR with radiosonde data, Martinet et al., 2022 found that air temperature has cold biases below 0.5 K in absolute value below 2 km but increases up to 1.5 K above 4 km altitude. The low biases in the lowest atmosphere allow a good estimation of the lowest temperature inversion under focus in this study. For each case study, the transition from stable to adiabatic fog is estimated using the static atmospheric stability in the lowest atmosphere computed using the temperature profile. The air temperature profiles are also used to characterize the atmospheric conditions linked to the development of fog at Charbonnière. For the absolute humidity, the maximum dry bias of the MWR is around 1.4 g m^{-3} in the lowest troposphere up to 1.7 km and becomes wet above (0.3 g m^{-3}). Martinet et al., 2022 showed that the LWP accuracy has been validated in clear-sky conditions and has shown errors between 1 and 14 g m^{-2}. These error range is in the scope of those defined in the literature (Crewell and Löhnert, 2003; Marke et al., 2016). The LWP is a key parameter to consider for the microphysical characteristics of fog and is used in the conceptual model. More information regarding the data can be found in Martinet, 2021.

The WindCube lidar has become a common instrument used in documenting very low atmospheric phenomena such as turbulence (Liao et al., 2020; Kumer et al., 2016). Dias Neto et al., 2023 demonstrated the usefulness of the wind speed and direction estimated using the WindCube V2. Comparing wind from WindCube V2 with GPS radiosonde, they found low biases of 0.52 m s^{-1} and 0.37° for the wind speed and direction, respectively. To investigate the dynamics of the atmosphere at the supersite, a WindCube V2 lidar manufactured by Leosphere was deployed by Meteo-France during the field campaign to provide from 1 October 2019 to 10 April 2020, the wind measurements at 10 levels ranging from 40 m to 220 m above ground level (a.g.l). The measurements made at a 1 Hz frequency and a 20 m vertical resolution provided the estimation of turbulence parameters such as the turbulent kinetic energy (TKE). The wind component are

estimated every 10 minutes using a Carrier-to-Noise Ratio (CNR) at least -23 dB and a total data availability of at least 50 %. Note that the CNR depends on atmospheric turbulence characteristics and relative humidity (Aitken et al., 2012). In the presence of fog or low stratus, the Lidar vertical range becomes low. The TKE is computed as the sum of the horizontal variances as in Kumer et al., 2016. Velocity variances are estimated every 30 minutes using the wind components at the high resolution. It is used in this study to analyze the role of turbulence within the foggy-layer to further characterize fog formation, evolution, and dissipation. More details on the WindCube lidar data can be found in Canut et al., 2022.

2.1.4 Fog adiabaticity and reservoir

To further understand fog characteristics, it is essential to focus our analysis on several variables related to the formation, evolution and dissipation of fog. Fog adiabaticity and reservoir are key metrics driving the life cycle of fog. They are estimated using the fog conceptual model (Toledo et al., 2021) developed at SIRTA. This model is a uni-dimensional model inspired by previous numerical models for stratus clouds (Betts, 1982, Albrecht et al., 1990; and Cermak and Bendix, 2011). The basic hypothesis is to consider a well-mixed fog layer and to express the increase in height of the fog liquid water content as a function of the local adiabaticity and the negative of the change in the saturation mixing ratio with height ($\Gamma_{ad}(T,P)$) (equation A1). Fog liquid water path is parameterized as a function depending on the equivalent fog adiabaticity (α_{eq}) and the CTH (equation A3). The equivalent fog adiabaticity is used to characterize the buoyancy in low clouds. α_{eq} varies depending on the in-cloud mixing parameter β and is expressed as $\alpha_{eq} = (1-\beta)$ (Betts, 1982 and Cermak and Bendix, 2011). For low-level clouds, as stratus and stratocumulus, α_{eq} is between 0.6 and 0.9 (Braun et al., 2018) indicating sufficient buoyancy in the cloud layer with an adiabatic profile. To parameterize this parameter in the fog conceptual model, Toledo et al., 2021 used an inversion of Eq. (A3) to define a fog adiabaticity from closure ($\alpha_{eq}^{closure}$) given as:

$$\alpha_{eq}^{closure} = \frac{2\left(LWP - LWC_0 CTH\right)}{\Gamma_{ad}\left(T,P\right)CTH^2} \tag{1}$$

$\alpha_{eq}^{closure}$ depends on the accumulated liquid water content (LWC) at the fog base (LWC_o), fog thickness (e.g. CTH), the LWP and the adiabaticity. The adiabaticity lapse rate is a function of air temperature and pressure. Toledo et al., 2021 found that the equivalent fog adiabaticity from closure is negative when the LWP is below 30 g m^{-2}. They defined the transition phase from stable to adiabatic conditions when the equivalent fog adiabaticity from closure is around 0.5. In the conceptual model, this parameter is estimated only for a CTH below 462.5 m with free cloud above.

231   The model considers that the fog dissipates when its liquid water path is below a certain

232   threshold depending on the local thermodynamic atmospheric conditions. In case of dissipation by

233   lifting the base height of the fog, Wærsted, 2018 found a deficit in LWP in the fog layer. This

234   assertion allows defining a minimum amount of LWP necessary to maintain the horizontal visibility

235   at surface lower or equal to 1000 m, defined as the critical liquid water path (CLWP). Thus, based

236   on equation A3, the CLWP can be expressed in equation (2) considering a critical liquid water

237   content at surface (LWCc).

238    $$CLWP = \frac{1}{2}\alpha_{eq}\Gamma_{ad}(T,P)CTH^2 + LWC_c CTH \qquad (2)$$

239   Theoretically, the LWCc corresponds to the LWC that would cause a 1000 m visibility. It is

240   estimated from the parameterization of Gultepe et al., 2006 based on the horizontal visibility at

241   surface.

242   Considering that adiabatic fog exists because the liquid water path in its thickness is strictly

243   greater or equal to its CLWP (Toledo et al., 2021), it is possible to define an associated quantity

244   named the fog reservoir of liquid water path (RLWP). The RLWP is defined as the difference

245   between fog current liquid water path and the critical value, as:

246    $$RLWP = LWP - CLWP = LWP - \frac{1}{2}\alpha_{eq}\Gamma_{ad}(T,P)CTH^2 - LWC_c CTH \qquad (3)$$

247   The RLWP depends on the LWCc (A4), the adiabaticity and fog thickness. The calculation of

248   RLWP can be used to anticipate the dissipation or thickening of the fog in the coming minutes or

249   hours. Based on 20 fog cases at SIRTA, Toledo, 2021 found that for a RLWP > 30 g m^{-2} in a given

250   time instant, fog does not dissipate within the following 30 minutes. He also showed that the RLWP

251   trend decreases before fog dissipation time and increases when fog is persisting. This behaviour

252   motivates the analysis of the RLWP trend in this study to improve the characterization of the

253   different fog phases.

254   The number of fog events observed during the SOFOG3D field campaign is not sufficient to

255   calibrate the fog conceptual model in southeastern France as in SIRTA (Toledo et al., 2021). In this

256   study, we use the model with its parametrization at SIRTA to further characterize the different

257   phases observed in the lifetime of fog based on identified case studies. The model is performed

258   when the visibility is lower than 1000 m. $\alpha_{eq}^{closure}$ is used to characterize the fog transition from

259   stable phase to adiabatic phase. The RLWP gives an estimation of the excess/deficit of liquid water

260   of the fog that enables the fog layer to remain at surface or dissipate. It can be used as a diagnostic

261   of how likely the fog will persist in the coming minutes, hours (nowcasting tool for fog dissipation

262 time). More details on the fog conceptual model is given in appendices and can be found in Toledo,
263 2021.

2.2 Case studies and methodological approach

265 For the whole SOFOG3D campaign, based on the fog defined criteria described in section
266 2.2.1, 31 fog events are identified during 31 October 2019 - 26 March 2020 period. For each one, a
267 visual inspection of the time-height cross-section of the radar reflectivity from BASTA cloud radar
268 and the cloud base height from the Ceilometer was carried out. We selected the four most
269 developed fog episodes, namely case studies 1 (IOP 5), 2 (IOP 6), 3 (IOP 11) and 4 (IOP 14).

270 As in Toledo et al., 2021 (their Fig. 3), Figure 2 shows the equivalent adiabaticity by closure
271 versus LWP and CTH for the 4 fog case studied. It indicates that $\alpha_{eq}^{closure}$ reaches 0.5 when LWP >
272 20 g m^{-2} and the CTH > 150 m which should be the conditions favorable for the fog to become
273 optically opaque to the infrared radiation. At the supersite, the LWP observed during that transition
274 is lower than the threshold at SIRTA (LWP > 30 g m^{-2}) (Wærsted et al., 2017 and Toledo et al.,
275 2021). However, there is a consistency between both sites on the computation of the equivalent
276 adiabaticity by closure. This legitimises the choice of the four days, and motivates the use of the
277 $\alpha_{eq}^{closure}$ in this study to define the transition phase between stable and adiabatic fog.

278 For the selected case studies, Table 1 contains the fog formation and dissipation times, fog
279 formation types, and fog duration at the supersite. For all selected fog events, the formation time of
280 fog is observed between 20:40 and 22:40 UTC and the dissipation time varies from night to
281 daytime. These selected fogs are triggered by radiation (2 cases) or advection-radiation (2 cases)
282 processes.

283 For each selected case study, temperature profiles from the MWR, radar reflectivity profiles
284 from the BASTA cloud radar and the equivalent fog adiabaticity derived from the conceptual model
285 are used to define the four fog phases characterizing the fog evolution: fog pre-onset, stable fog,
286 adiabatic fog, and fog dissipation. Note that an important time of the fog life cycle is the transition
287 time between stable and adiabatic fog. Each fog phase is defined as following:

288 1/ Fog pre-onset corresponds to the two hours preceding fog onset associated with cloud free
289 conditions.

290 2/ In the four cases studies, the stable phase starts at fog onset. It is characterized by a stable
291 temperature profile in the lowest 100 m of the atmosphere.

292 3/ The transition time separating the stable and adiabatic phases can be defined differently
293 depending on the meteorological variables considered. Price et al., 2011 defined this transition time
294 as the time when the air temperature becomes constant in the fog lowest layer (1.5 - 50 m a.g.l).

Toledo et al., 2021 found that the transition is observed when the equivalent fog adiabaticity by closure is increasing between 0 and 0.5. In this study, for a better definition of this period, we take into account the static stability given by the hourly profiles of mean air temperature from the MWR, the fog geometry (CTH) from the cloud radar, and the $\alpha_{eq}^{closure}$ from the conceptual model. Indeed, the transition period is defined as the time when the temperature profile becomes unstable or neutral in the 0-75 m a.g.l layer, while the fog CTH increases with time, and $\alpha_{eq}^{closure}$ increases from 0 to about 0.5. Note that the thickening of the fog is associated with the elevation of the level of the maximum radar reflectivity. The transition phase starts when $\alpha_{eq}^{closure} < 0.5$, the CTH suddenly increases more than 25 m in 5 minutes under a stable or neutral layer. This phase ends when $\alpha_{eq}^{closure}$ reaches 0.5 and the fog layer becomes neutral or unstable.

4/ Fog adiabatic phase is characterized by $\alpha_{eq}^{closure}$ around 0.5, a neutral or unstable temperature profile, and a radar reflectivity that increases with increasing altitude and peaks a few tenths of meters below cloud top.

5/ Fog dissipation phase is defined as being the period between 30 minutes before and after dissipation time (when horizontal visibility becomes greater than 1 km). Since the fog dissipation time does not appear abruptly, as it is also driven by thermodynamical processes, we consider this time range to further document them.

Based on these fog phase definitions, in the following, we describe the four case studies. For each fog event, we document the processes involved in the evolution of fog in each of these phases, using the fog conceptual model and the instrumental synergy, in order to identify the main processes driving the fog life cycle.

Table 1 : Case study number, fog onsets, type of fog formation, fog dissipation times, fog duration and type of fog dissipation for the four documented case studies. Time is in UTC. Dates are in the format "dd/mm/yyyy". "dd" indicates the day, "mm" the month and "yyyy" the year.

Case study number	Formation time		Fog types	Dissipation time		Fog duration (hh:min)
	Date dd/mm/yyyy	Hours (UTC)		Date dd/mm/yyyy	Hours (UTC)	
1	28/12/2019	22:40	Radiation	29/12/2019	11:00	12:20
2	05/01/2020	20:40	Radiation	06/01/2020	08:40	12:00
3	08/02/2020	20:40	Advection-radiation	09/02/2020	03:40	7:00
4	07/03/2020	21:20	Advection-radiation	08/03/2020	04:00	6:40

3. Fog formation, evolution, and dissipation processes

3.1 Radiation fog case studies

3.1.1 Case study 1 (IOP 5) analysis

Figures 3a and 3b indicate the time-cross sections of the radar reflectivity estimated from BASTA cloud radar during case study 1, on the 28-29 December 2019, respectively up to 600 m and 12000 m. They show a clear sky before fog formation time at 22:40 UTC on 28 December 2019. During fog evolution, cloud free conditions are observed above the fog top height until 09:00 UTC when sparse thin high-altitude clouds occur above the cloud radar. Figure 3c presents a quasi-homogeneous fog formation time between the three sites and heterogeneous dissipation time. At Charbonnière, fog dissipated at 11:00 UTC, on 29 December 2019 and two hours earlier at Noaillan. At all sites, low temperatures below 4 °C (Fig. 3e) are observed during the fog period. Near the surface, light winds (< 1 m s^{-1}) are recorded at all sites from fog pre-onset to fog stable/adiabatic transition times (Fig. 3d and 3f).

The fog pre-onset is marked by a double stratification of the atmospheric boundary layer with a thin inversion from surface up to 100 m and deep and strong inversion (around 8 °C km^{-1}) above (Fig. 4a). Atmospheric conditions are dominated by an easterly wind that reaches 5 m s^{-1} above 100 m a.g.l which could be considered as a nocturnal low-level jet (Fig. 4d). The mean cooling rate near the surface is -0.9 °C h^{-1}. The strong decrease in temperature is associated with a negative SHF (-0.23 W m^{-2}) (Fig. 4h), near surface low wind (0.61 m s^{-1}) (Fig. 3d and 3f) and low turbulence (TKE = 0.11 m^2 s^{-2} and σ_w^2 = 0.002 m^2 s^{-2}). These conditions lead to thermally-stable atmospheric conditions which are favourable for radiation fog formation (Table 1).

The fog stable phase lasts around 6 h (22:50 - 05:00 UTC) and is characterized on average by a very low negative near surface cooling rate (-0.18 °C h^{-1}), an almost zero SHF, an easterly light wind (0.78 m s^{-1}), low turbulence (TKE = 0.07 m^2 s^{-2}, σ_w^2 = 0.01 m^2 s^{-2}), negative $\alpha_{eq}^{closure}$ (-1.3) (Fig. 4e), low LWP (2.18 g m^{-2}) (Fig. 4g), slight increase in time of the fog thickness up to 50 m, and relatively stable temperature inversion height. These characteristics maintain the fog thermally stable with an horizontal visibility of 736 m on average.

The transition time from stable to adiabatic fog is observed between 05:00 and 07:00 UTC (02:00 duration) and associated with a lowest visibility (198 m), a transition in the vertical profiles of air temperature (Fig. 4a) from stable at 05:00 to unstable at 06:00 UTC in the fog layer, a deepening of the cold layer, an increase of the mean SHF reaching 4.4 W m^{-2} and around 10 W m^{-2} at the phase end (Fig. 4h), an increase of the turbulence (TKE up to 0.15 m^2 s^{-2} and σ_w^2 up to 0.04 m^2 s^{-2}) generated by the strengthening of the wind speed (1.14 m s^{-1}) and its shift in direction from East to Southeast. From 05:00 to 06:00 UTC, the coldest temperature shifts from the surface up to 50 m

a.g.l, the vertical profile of radar reflectivity increases with height, indicating a vertical development of fog (Fig. 4b) generated by turbulence processes. At the end of this phase, $\alpha_{eq}^{closure}$ reaches 0.5 which is consistent with the threshold obtained at the SIRTA site by Toledo et al., 2021. σ_w^2 values observed are higher than the threshold fixed by Price et al., 2019 for a thermally-stable surface layer. The LWP (28 g m^{-2}) and RLWP (+15 g m^{-2}) peak at the end of the transition phase consistently with a decrease in visibility. Due to the simultaneous increase in SHF, TKE and σ_w^2, the transition phase is driven by both thermal and mechanical turbulence.

The fog adiabatic phase is observed between 07:00 and 11:00 UTC (04:00 duration) at the supersite and characterized by a vertical development of fog up to 187.5 m (Fig. 4b) and the arrival of sparse high clouds (Fig. 3a and 3b) associated with the lowering of the temperature inversion top height above the fog top (Fig. 4c). Note that these clouds have no effect on the radiative cooling at the top height of the fog. The fog layer becomes warmer (+0.77 °C h^{-1} on average) and its LWP and RLWP reach 26.16 g m^{-2} and +6.38 g m^{-2}, respectively. The turbulence gradually increases in the fog layer (Fig. 4f) (TKE = 0.23 m^2 s^{-2}) due to an increase of the horizontal wind speed (2.4 m s^{-1}) combined with an increase of the vertical shear and the wind shift from southeasterly to easterly (Fig. 4d). In the same way, σ_w^2 increases to 0.04 m^2 s^{-2} and is driven both by the vertical wind shear and the increase in SHF (12.9 W m^{-2}) (Fig. 4h). For this case study, the moderate mechanical and thermal turbulence causes the vertical mixing in the fog layer, which slightly increases the surface horizontal visibility (370 m) and fog top height (185 m).

At the supersite, in the absence of any cloud above the fog layer, the fog dissipates after sunrise. It is marked by a continue increase in SHF (Fig. 4h) due to solar radiation (daytime atmospheric convection), negative RLWP (-11.39 g m^{-2}), an increase in CTH (290 m), LWP (maximum of 43.34 g m^{-2}), stable $\alpha_{eq}^{closure}$ around 0.63, and more thermal turbulence ($\sigma_w^2 = 0.06$ m^2 s^{-2}) allowing more vertical mixing. Based on the RLWP, the fog conceptual model would predict a deficit of liquid water in the fog layer one hour before the lifting of its base height (Fig. 4g). The fog dissipation phase is induced by the increase of the vertical mixing generated by the thermal (solar heating) and mechanical turbulence associated with TKE values larger than 0.4 m^2 s^{-2} (Fig. 4f).

In summary, for this radiative fog event, the fog conceptual model is consistent with the in-situ measurements of turbulence on the timing of the different fog phases. It has provided additional elements for understanding the different phases of the fog life cycle.

3.1.2 Case study 2 (IOP 6) analysis

384   As in case study 1, case study 2 is a radiation fog that forms under clear skies a few hours

385 after sunset (Fig. 5a and 5b), under a double stratification of the low atmosphere (Fig. 6a), southerly

386 very low near-surface wind speed (0.2 m s^{-1}), low TKE (0.06 m^2 s^{-2}) and negative surface SHF. The

387 fog lasts 12 h and completely dissipates around 08:40 UTC, on 6 January 2020 at the supersite (see

388 Table 1) and at 04:30 UTC at Noaillan revealing more spatial variability than in case study 1.

389   The fog stable phase last 3 h 20 min (20:40 to 00:00 UTC), half the time of case study 1,

390 with fog characteristics similar to those of case study 1. A 2-hour fog transition phase is observed

391 from 00:00 to 02:00 UTC, (02:00 duration as for IOP 5) at the supersite (Fig. 6a and 6b) and

392 characterized by positive SHF (7.76 W m^{-2}) and larger values of TKE (0.23 m^2.s^{-1}) allowing vertical

393 mixing and transition towards adiabatic fog. A significantly longer fog adiabatic phase is observed

394 from 02:00 to 08:40 UTC (twice longer than in IOP 5). The first period from 02:00 to 05:00 UTC is

395 characterized by continued positive SHF (10 W m^{-2}) (Fig. 6h) and significant turbulence (TKE > 0.2

396 m^2 s^{-2} and σ$_w^2$ > 0.02 m^2 s^{-2}) (Fig. 6f) leading to a deeper fog with relatively high LWP (42 g m^{-2}), and

397 a positive RLWP until 04:30 UTC (Fig. 6g). The second period from 05:00 to 08:40 UTC is

398 characterized by continued positive SHF, significant σ$_w^2$ (> 0.02 m^2 s^{-2}), while the TKE decreases (<

399 0.2 m^2.s^{-2}) associated with the decrease in wind speed in the fog layer. A sharp decrease in LWP,

400 with a reduction of fog top height leads to RLWP oscillating around 0 g m^{-2}, while the horizontal

401 visibility increases and then decreases again. During this period, the sharp decrease in LWP (< 20 g

402 m^{-2}) results in a fog layer that is not very resilient to the significant turbulence, as shown by the very

403 low RLWP values and rapidly changing horizontal visibility (Fig. 5c). The decrease in LWP could

404 be driven by production of drizzle, as scientist reported droplet freezing on the tethered balloon. Fog

405 dissipation occurred after sunrise (08:40 UTC), under positive SHF (14 W m^{-2}), driven by the

406 turbulence associated with mechanical and thermal processes (mean TKE ~ 0.28 m^2 s^{-2} and σ$_w^2$

407 ~0.048 m^2 s^{-2}).

3.2 Radiation-advection fog case studies

409 Case study 3 and 4 correspond to two fog cases that form after sunset (near 21 UTC) in a moist

410 westerly flow, with an initial condensation about 100 m a.g.l (ultra-low stratus or elevated fog)

411 followed by a rapid subsidence of the cloud layer to the ground (see Figures 7 and 9, respectively).

412 West-east gradients are observed in terms of temperature and fog formation time, combined with a

413 weak temperature inversion at the time of fog formation, justifying the classification of fog

414 formation by advection-radiation processes (Ryznar, 1977).

3.2.1 Case study 3 (IOP 11) analysis

416   In spite of different formation conditions for case study 3, compared to case 1 and 2, the stable fog

417   phase of this case is characterized by fog conditions that are similar to those of case 1 and 2 (Figure

418   8): slightly negative SHF, low turbulence (TKE = 0.03 $m^2 s^{-2}$) and low LWP (<10 $g\ m^{-2}$). Case study

419   3 differs from the previous case studies with a longer duration for the stable-to-adiabatic fog

420   transition (03:30 duration) during which SHF remains slightly negative, TKE remains mostly below

421   0.03 $m^2\ s^{-2}$, and CTH, LWP and $\alpha_{eq}^{closure}$ increase progressively, while RLWP remains relatively

422   stable (5-10 $g\ m^{-2}$). In case study 3, the very short fog adiabatic phase (1 hour) is characterized by

423   increasing vertical wind shear near fog top height (Fig. 8d) that generates dynamical instability

424   driving the vertical mixing, reducing the temperature inversion above fog top (Fig. 8c), and

425   promoting vertical development of the fog layer. The rapid increase in CTH is not sufficiently

426   compensated by the increase in LWP, leading to a decrease in RLWP (Fig. 8g) and subsequent

427   increase in near-surface visibility and dissipation of the fog. Increasing wind aloft brings warm drier

428   air over the top of the fog that then mixing into it (TKE = 0.33 $m^2\ s^{-2}$ and σ_w^2 = 0.07 $m^2\ s^{-2}$),

429   evaporating fog droplets, reducing the RLWP to negative values and causing the fog to lift into low

430   stratus. The fog dissipation phase is thus driven by the advection of warm air at the supersite (Fig.

431   7e).

3.2.2 Case study 4 (IOP 14) analysis

433   As in case study 3, fog case study 4 starts with a very low stratus fog, subsidence of the

434   cloud layer resulting in a fog. The fog layer is perturbed by the advection from the northwest

435   (captured in Meteosat Second image, not shown) around 00:30 UTC of another stratus with a base

436   height above the fog top height. From 04:00 UTC, the fog becomes intermittent with a first

437   dissipation observed at that time and a definitive dissipation around 07:00 UTC.

438   The 2-hour long fog stable phase is also characterized by a cooling rate near -1°C h^{-1}, slightly

439   negative SHF and low turbulence (TKE < 0.1 $m^2 s^{-2}$). The relatively short transition from stable to

440   adiabatic fog (< 1 h 30 min) is characterized by an increase in mechanically-driven turbulence

441   (wind shear, Figure 10d) with a southerly wind that likely brings additional moisture, leading to a

442   rapid increase in both CTH and LWP (near 40 $g\ m^{-2}$).

443   Fog adiabatic phase is observed from 00:20 to 04:00 UTC (03:40 duration) followed by a

444   temporary dissipation of the fog from 04:00 to 05:30 UTC and a definitive fog dissipation at 07:00

445   UTC. This adiabatic phase is characterized by a 250-300 m deep fog with 40-50 $g\ m^{-2}$ LWP. The

446   mechanically driven TKE ranges between 0.2-0.4 $m^{-2}\ s^{-2}$ (Figure 10f) which confirms the turbulence

447   that a relatively deep fog layer can withstand. The evolution of RLWP to negative values after

448   04:00 UTC (Figure 10g) shows that the conceptual model captures the transition from an adiabatic

449 fog with low near-surface visibility (< 300 m) to one with horizontal visibility at or above 1000 m

450 (Figure 9c). The definitive dissipation is not associated with increasing turbulence, but rather with

451 the presence of middle-altitude clouds that likely reduce significantly the fog top radiative cooling,

452 as precisely characterized by Waersted et al. (2017), and hence liquid water content production.

453 Indeed, Figure 10g reveals a significant LWP reduction after 6:30 UTC, that explains the definitive

454 dissipation of the fog before sunrise.

455 **4. Discussion**

456   Figure 11 shows the mean vertical profiles of air temperature derived from the MWR and

457 radar reflectivity measured by the cloud radar for each fog phase and each case study. It highlights

458 the thermal and microphysical characteristics of fog phases and differences in atmospheric

459 conditions between fog categories: radiation and radiation-advection fogs.

460   For radiation fog case studies (1 and 2), fog develops below the dry, warm and cloud free

461 stable atmospheric boundary layer (Fig. 4c and 6c). Atmospheric conditions preceding (two hours

462 before) fog formation are dominated by a strong and thick temperature inversion (more than 14 °C

463 and 1000 m) which is associated with anticyclonic conditions over Europe favouring easterly wind

464 and clear sky across the studied area. These atmospheric conditions allow a strong surface radiative

465 cooling, negative heat fluxes and cooling of near surface air at a rate of -0.9 and -0.7 °C h^{-1} for case

466 study 1 and 2, respectively. This cooling is associated with low turbulence indicated by low values

467 of TKE (0.18 $m^2 s^{-2}$ in case 1, and 0.06 in case 2) and near surface vertical velocity variance (σ_w^2 <

468 0.003 $m^2 s^{-2}$) which reinforce the surface thermally stable boundary layer (Fig. 11a and 11b)

469 favoring the triggering of radiation fog. These results are consistent with the definition of radiation

470 fog proposed by Price, 2019.

471   In advection-radiation fog case studies (3 and 4), two hours before fog formation, a westerly

472 sea breeze is present, transporting mild wet air from the ocean. Surface heat fluxes are negative,

473 favoring cooling of the near-surface air (-1 °C h^{-1} in case study 3 and -0.5 °C h^{-1} in case study 4) and

474 turbulent mixing is low (TKE < 0.06 $m^2 s^{-2}$). An East-West gradient of formation and dissipation is

475 observed in line with the westerly synoptic advection of Atlantic inflow. Fog forms earlier in the

476 West and dissipates later in the East. The combination of advection and radiative cooling favours

477 stratus fog formation at about 150 m a.g.l followed by a rapid (less than 30 min) lowering of it base

478 height to the surface triggering the onset of the fog in an unstable (case 3) and neutral (case 4)

479 surface atmospheric boundary layer (Fig. 11c and 11d).

480   The stable fog phase is characterized by a stable temperature profile and radar reflectivity

481 which is maximum near the surface and decreases with height (see Fig. 11). The fog remains

482   shallow (less than 100 m) with a low LWP ranging less than 12 g m^{-2} proportional to fog depth

483   (Table 2). The equivalent fog adiabaticity by closure parameter ($\alpha_{eq}^{closure}$) is typically negative during

484   the stable phase indicating that the fog is not in an adiabatic phase. The near-surface temperature

485   decreases very moderately (-0.2 °C h^{-1}) in cases 1 and 2, while the air keeps cooling at about -1 °C

486   h^{-1} in cases 3 and 4. For the four cases, surface heat fluxes are slightly negative (-3 to 0 W m^{-2}) and

487   turbulence remains low (TKE at about 0.1 m^2 s^{-2} and σ_w^2 at 0.01 m^2 s^{-2}). This phase is characterized

488   by very low LWPs (1-2 g m^{-2} for radiation fogs and 6-11 g m^{-2} for advection-radiation fog). For

489   radiation fog cases, the stable phase lasts around 6 and 4 hours, respectively, while for advection-

490   radiation cases, it lasts around 2 hours. This is consistent with the strength of the surface inversion

491   of each category of fog, as shown in Figure 11. These macrophysical characteristics of the fog

492   stable phase are consistent with those found by Toledo et al., 2021.

493   The transition from stable to adiabatic phases is a key period in the fog life cycle. This

494   period is well characterized using the macrophysical parameters of the conceptual model, namely

495   the equivalent fog adiabaticity by closure ($\alpha_{eq}^{closure}$) parameter of the fog, the fog geometry (CTH)

496   and fog LWP. During the transition from stable to adiabatic phases, these three parameters increase

497   significantly (see Table 2). In particular, $\alpha_{eq}^{closure}$ evolves progressively from negative values towards

498   +0.5 (Toledo et al., 2021). The transition phase lasts from 1 h 30 min to 3 h 30 min, however its

499   timing of occurrence is quite variable (case 1 at (05:00 - 07:00 UTC), case 2 (00:00 - 02:00 UTC),

500   case 3 (23:00 - 02:30 UTC), and case 4 (23:30 - 01:00 UTC). During this phase, a change is

501   observed in static stability from stable profiles to neutral adiabatic profiles (Fig. 11), while the radar

502   reflectivity profile presents maximum values near the ground that decrease with height (Fig. 11). In

503   cases 1, 2 and 4, the transition phase is characterized by an increase in turbulence that can explain

504   the decrease in thermal stability of the fog layer, either shown in the vertical velocity variance (σ_w^2

505   >= 0.02 m^2 s^{-2}) associated with positive surface heat fluxes (cases 1 and 2), or TKE exceeding 0.3

506   m^2 s^{-2} (cases 2 and 4). In all the cases, the fog LWP increases significantly which allows a more

507   efficient radiative cooling of the fog layer, hence contributing to the destabilization of the fog layer.

508   In case 3, the transition phase is not marked by a significant increase in turbulence. The transition is

509   more progressive than in the other case studies, with gradual increases of CTH, LWP and $\alpha_{eq}^{closure}$

510   during this long phase (03:30 duration).

511   According to temperature vertical profiles from the MWR, at the end of the transition time

512   from stable to adiabatic fog, the temperature profile becomes neutral or slightly unstable. This is

513   consistent with the definition of the transition given by Price et al., 2011. We also find that it is

514   during this period that the fog reaches its maximum value of RLWP, showing that the LWP

increases beyond the critical liquid water path value, which gives information on the persistence of fog.

For radiation fog case studies, the adiabatic phase lasts 04:00 and 06:40 hours for case 1 and 2 respectively, maintaining the fog life cycle during the night until after sunrise. In cases 3 and 4, the adiabatic phase is shorter and lasts 01:00 and 03:40 hours, respectively, with a night-time dissipation at 03:40 and 04:00 UTC, respectively. In this fog phase, for radiation fog, the LWP ranges from 22-26 g m^{-2} with CTH near 187.5 m a.g.l. The fog is deeper for advection-radiation fog cases with LWP / CTH at 30 g m^{-2} / 200 m a.g.l and 43 g m^{-2} / 287.5 m a.g.l, respectively (Table 2). The adiabatic phase is characterized by an equivalent fog adiabatic closure parameter near or above 0.5, and a positive yet low RLWP. For all the cases except case 3, the adiabatic phase is associated with moderate turbulence in the fog layer ($0.2 <$ TKE < 0.4 m^2 s^{-2} and $0.03 < \sigma_w^2 < 0.04$ m^2 s^{-2}) which indicates significant vertical mixing generating an unstable surface atmospheric boundary layer (Fig. 11). This finding is consistent with the result of Ju et al., 2020 who based their analysis on one case study and Ghude et al., 2023, Dhangar et al., 2021 and Zhou and Ferrier, 2008 for more case studies analysis. In addition, this phase can also be driven by horizontal advection (mesoscale and synoptic systems) as in the case study 3.

This study shows two distinct fog dissipation periods, at night and after sunrise. Daytime dissipation is observed for radiative fog cases and night-time dissipation for advection-radiation ones. All of them are observed when $\alpha_{eq}^{closure} > 0.5$, TKE > 0.3 m^2 s^{-2}, $\sigma_w^2 > 0.04$ m^2 s^{-2}, and the LWP > 40 g m^{-2} (except case study 2). For cases 1 and 2, turbulence is thermally driven by positive SHF, while for cases 3 and 4, the night-time turbulence increase is mechanically driven by increased wind speed. For all case studies, the RLWP decreases significantly from the stable phase to the dissipation phase, confirming that dissipation through fog-base lifting is linked to insufficient liquid water content in the fog layer, as suggested by the conceptual model. For case 3, the RLWP becomes negative 20 min after dissipation. This delay is likely due to very rapid changes in LWP and CTH at the fog dissipation time.

5. Summary and Conclusions

The SOFOG3D field campaign provides a unique dataset documenting thermodynamic and dynamical atmospheric circulations to further understand the processes driving fog formation and dissipation over Southeastern France. Based on an innovative instrumental synergy combining in-situ and remote sensing measurements, combined with an adiabatic fog conceptual model, this study documented key processes and conditions such as advection, turbulent mixing, radiative cooling, atmospheric stability, fog water content and depth, presence of clouds above. We analysed

548 the role of these processes and impacts of these conditions on fog formation, evolution and

549 dissipation, focusing on four fog case studies: two radiation and two advection-radiation fogs. For

550 each case study, we defined the different phases characterizing the fog life cycle, namely (i) its

551 formation, (ii) an initial phase where the fog develops under thermally stable conditions, (iii) a

552 transition phase towards an adiabatic fog, (iv) an adiabatic phase during which the fog vertical

553 profile is adiabatic, and (v) a dissipation phase where the fog base lifts.

554   The results showed that for both radiation fog cases, the conditions are marked by very cold

555 atmospheric conditions associated with a continental easterly nocturnal low-level jet. For these

556 cases, the stable fog phase develops under strong surface radiative cooling and weak turbulence, in

557 a deep temperature inversion layer. The stable phase lasts as long as the wind speed and turbulence

558 remain very low (typically 1 m s^{-1} and 0.1 m^2 s^{-2}). The transition phase is driven by an increase of

559 wind speed and turbulence in the fog layer, reaching 2 m s^{-1} and 0.2 m^2 s^{-2}, respectively. This

560 increased turbulence is of mechanical origin (increased wind shear associated with an evolution of

561 the airmass) hence its time of occurrence varies widely from one case to the other (05 and 00 UTC,

562 respectively). The adiabatic phase is characterized by sustained turbulence (0.2 < TKE <0.4 m^2 s^{-2})

563 sufficient to ensure vertical mixing in the fog layer. The fog layer is then typically deeper than 100

564 m, and the LWP exceeds 20 g m^{-2}. For these fog events, dissipation time is observed after sunrise,

565 when both thermal and dynamic production of the turbulence are high (TKE > 0.4 m^2 s^{-1} and σ_w^2 >

566 0.04 m^2 s^{-2}). For both fog cases, we observe simultaneous increase of near-surface visibility and

567 decrease of the fog LWP reservoir (RLWP) derived from the fog conceptual model, about one hour

568 before dissipation time.

569   The analysis on the advection-radiation case studies shows that they have the shortest life

570 cycle linked to the low surface boundary layer stability, because they occur under westerly air

571 masses that evolved during the night (change in wind direction, increased wind shear). In this

572 category of fog, the processes driving the stable, stable/adiabatic transition and adiabatic phases are

573 similar to those of the radiation fog category. However, in one case, we observe a transition phase

574 that occurs with a more subtle increase in turbulence than in the other three cases. As a result, the

575 increase in LWP and CTH is very slow; it takes more than 3 hours to reach adiabatic conditions.

576 Dissipation occurs before sunrise in both cases. In one case it is due to a sudden increase in wind

577 speed and wind shear leading to TKE values exceeding 0.4 m^2 s^{-1}. In the other case, we have a deep

578 adiabatic fog (CTH > 200 m) with sustained turbulence (0.2 < TKE <0.4 m^2 s^{-2}) where the LWC

579 production is barely sufficient to maintain the fog all the way down to the surface. The conceptual

580 model shows negative RLWP values, while the visibility oscillates around 1 km. The full

581 dissipation of the fog is here associated with the presence of a cloud above the fog that further
582 reduces the LWC production.

583   In summary, this paper provides quantitative analyses of key parameters and conditions that
584 drive the fog life cycle. The level of turbulent mixing in the fog, of both thermal and mechanical
585 origin is key to understand important transitions (from stable to adiabatic, and from adiabatic to
586 dissipation). This level of turbulence should be analysed considering the depth of the fog and its
587 liquid water path. Our study confirms that the RLWP, combined with visibility is an interesting
588 parameter to study the state of the fog, even though LWP and RLWP measured during SOFOG3D
589 present lower values than at the SIRTA site, close to the uncertainty of the measurement. Fog
590 formation, evolution and dissipation across southern France require an analysis of the synoptic
591 atmospheric circulation in terms of wind, cloud cover, and thermodynamical processes. Indeed, this
592 paper highlights that fog nowcasting tools in this region needs in addition to the numerical weather
593 prediction models, a cloud radar, a microwave radiometer, a wind lidar, a surface energy balance,
594 and meteorological stations. Operationalizing these instruments would allow to improve fog
595 nowcasting, which will reduce its socio-economic impacts in this region.

596 **Appendix A: Fog conceptual model parametrization**

597 **A.1 Liquid water content**

598   The conceptual model for adiabatic fog has been developed at SIRTA by Toledo et al.,
599 2021. This model is a unidimensional model inspired by previous numerical models for stratus
600 clouds (Betts, 1982, Albrecht et al., 1990; and Cermak and Bendix, 2011) (see equation 1). The
601 basic hypothesis is to consider a well-mixed fog layer and express the increase with height of the
602 fog liquid water content as a function of the local adiabaticity ($\alpha(z)$) and the negative of the change
603 in the saturation mixing ratio with height ($\Gamma_{ad}(T,P)$), given in equation A1.

604 $$\frac{dLWC(z)}{dz} = \alpha(z)\Gamma_{ad}(T,P) \qquad\qquad\qquad (A1)$$

605   Where T and P are air temperature and pressure, respectively. z is the height above the
606 surface and varies between 0 and the cloud top height (CTH). By integrating equation 1, it is
607 important to take into account fog geometry which is different from that of the stratus cloud. For a
608 fog, the LWC at the base is non-zero due to the presence of liquid droplets down to the ground
609 level. This presence of droplets drives surface visibility reduction and water deposition on the soil.
610 Thus, as indicated in equation A2, the vertical integral of the LWC(z) is a function of the variation
611 with height of the adiabaticity, $\Gamma_{ad}(T,P)$ and the measurement of the LWC at surface (LWC_0). This
612 equation shows that the LWC increases with the thickness of the fog up to the height where upward

motions of moisture from the surface are constrained by downward motions of dry air from the fog top height (Walker, 2003; Cermak and Bendix, 2011). From this interface level, the LWC decreases with height and becomes zero at the fog top height (Brown and Roach, 1976; Cermak and Bendix, 2011).

$$LWC(z) = \int_{z'=0}^{z'=z} \alpha(z')\Gamma_{ad}(T,P)dz' + LWC_0 \qquad (A2)$$

A.2 Liquid water path

The fog liquid water path (LWP) represents the total amount of liquid water present in the fog layer. It can be estimated by integrating equation A2 in height considering that the fog thickness is equivalent to the CTH (equation A3). An approximation assuming a constant adiabaticity is introduced by using the equivalent fog adiabaticity term α_{eq}. This simplifies the calculation, since a complete computation would require a knowledge of the vertical profile of adiabaticity which depends on the thermodynamic properties of the fog layer. In this conceptual model, the LWC is treated as if it increased linearly with height from the surface to the CTH. At the surface level the LWC from the model and fog are the same, connecting a given LWP with surface LWC. This quantity is converted to visibility values using Gultepe et al., 2006 parametrization. Hence, the conceptual model connects fog LWP with its CTH and surface visibility values, it provides an estimation of the equivalent fog adiabaticity.

$$LWP = \frac{1}{2}\alpha_{eq}\Gamma_{ad}(T,P)CTH^2 + LWC_0 CTH \qquad (A3)$$

Data availability. All the data used in this study are hosted by the the French national center for Atmospheric data and services AERIS in the link https://sofog3d.aeris-data.fr/catalogue/#masthead. Data access can be free following the conditions fixed by the SOFOG3D project.

Competing interests. The authors claim no conflict of interest for this study.

Author contributions. **Cheikh DIONE:** Conceptualization, Methodology, Investigation, Validation, Formal-analysis, Writing – original draft, Writing – review & editing, Visualization. **Martial HAEFFELIN:** Supervision, Methodology, Investigation, Formal-analysis, Writing-original draft, Writing-review & Editing, , Funding acquisition. **Jean-Charles DUPONT:** Supervision, Investigation, Editing. **Felipe TOLEDO:** Methodology, Investigation, Editing. **Frederic BURNET:** Project administration, Resources, Investigation, Editing, Funding acquisition.

Christine LAC: Supervision, resources, Investigation, editing, Funding acquisition. **Jean-Francois RIBAUD:** Visualization, Investigation, Editing. **Pauline MARTINET:** Editing, Investigation, Data curation. **Guylaine CANUT:** Investigation, Editing, Data curation. **Susana JORQUERA:** Data curation. **Julien DELANOË:** Data curation.

Acknowledgments. The SOFOG3D field campaign was supported by METEO-FRANCE and ANR through grant AAPG 2018-CE01-0004. Data are managed by the French national center for Atmospheric data and services AERIS. The CNRM/GMEI/LISA team supported the deployment, monitoring and data processing and supplying of Wind lidar and microwave radiometer.

References

1   Aitken, M. L., Rhodes, M. E., Lundquist, J. K.: Performance of a Wind-Profiling lidar in the Region of WindTurbine Rotor Disks. J. Atmos. Ocean. Technol. 29, 347-355, https://doi.org/10.1175/JTECH-D-11-00033.1, 2012.

2   Albrecht, B. A., Fairall, C. W., Thomson, D. W., White, A. B., Snider, J. B., and Schubert, W. H.: Surface-based remote sensing of the observed and the Adiabatic liquid water content of stratocumulus clouds, Geophys. Res. Lett., 17, 89-92, https://doi.org/10.1029/GL017i001p00089, 1990.

3   Bartok J, Bott A, Gera M.: Fog prediction for road traffic safety in a coastal desert region. Bound-Layer Meteor., 145(3), 485-506, https://doi.org/10.1007/s10546-012-9750-5, 2012.

4   Bartoková I, Bott A, Bartok J, Gera M.: Fog prediction for road traffic safety in a coastal desert region: Improvement of nowcasting skills by the machine-learning approach, Boundary-Layer. Meteor., 157, 501-516, https://doi.org/10.1007/s10546-015-0069-x, 2015.

5   Bell, A., Martinet, P., Caumont, O., Burnet, F., Delanoë, J., Jorquera, S., Seity, Y., and Unger, V.: An optimal estimation algorithm for the retrieval of fog and low cloud thermodynamic and micro-physical properties, Atmos. Meas. Tech., 15, 5415–5438, https://doi.org/10.5194/amt-15-5415-2022, 2022.

6   Bergot T.: Small-scale structure of journal radiation fog: a large-eddy simulation study, Q. J. R. Meteor. Soc., 139(673):1099-1112, https://doi.org/10.1002/qj.2051, 2013.

7   Bergot, T., Escobar, J. and Masson, V.: Effect of small-scale surface heterogeneities and buildings on radiation fog: Large-eddy simulation study at Paris-Charles de Gaulle Airport, Q. J. R. Meteor. S., 141(686), 285-298, https://doi.org/10.1002/qj.2358, 2015.

8   Betts, A. K.: Cloud Thermodynamic Models in Saturation Point Coordinates, J. Atmos. Sci., 39, 2182-2191, https://doi.org/10.1175/1520-0469(1982)039<2182:CTMISP>2.0.CO;2, 1982.

673   9   Boutle, I., Angevine, W., Bao, J.-W., Bergot, T., Bhattacharya, R., Bott, A., Ducongé, L., Forbes, R.,
674   Goecke, T., Grell, E., Hill, A., Igel, A.L., Kudzotsa, I., Lac, C., Maronga, B., Romakkaniemi, S.,
675   Schmidli, J., Schwenkel, J., Steeneveld, G.-J. and Vié, B.: Demistify: A large-eddy simulation (LES)
676   and single-column model (SCM) intercomparison of radiation fog, Atmos. Chem. Phys., 22(1), 319-
677   333, https://doi.org/10.5194/acp-22-319-2022, 2022.

678   10 Braun, R. A., Dadashazar, H., MacDonald, A. B., Crosbie, E., Jonsson, H. H., Woods, R. K., Flagan,
679   R. C., Seinfeld, J. H., and Sorooshian, A.: Cloud Adiabaticity and Its Relationship to Marine
680   Stratocumulus Characteristics Over the Northeast Pacific Ocean, J. Geophys. Res. Atmos., 123,
681   13790-13806, https://doi.org/10.1029/2018JD029287, 2018.

682   11 Brown, R. and Roach, W.: The physics of radiation fog: II-a numerical study, Q. J. R. Meteor. Soc.,
683   102, 335-354, https://doi.org/10.1002/qj.49710243205,1976.

684   12 Burnet, F.: SOFOG3D_TUZAN_CNRM_CEILOMETER-CL51-30SEC_L1. [Dataset], Aeris.
685   https://doi.org/10.25326/241, 2021.

686   13 Canut, G.: SOFOG3D_CHARBONNIERE_CNRM_LIDARwindcube-TKE_L2. [Dataset]. Aeris.
687   https://doi.org/10.25326/323, 2022.

688   14 Canut,   G.:   SOFOG3D_JACHERE_CNRM_TURB-30MIN_L2.   [Dataset].   Aeris.
689   https://doi.org/10.25326/91, 2020.

690   15 Canut,   G.:   SOFOG3D_JACHERE_CNRM_TURB-30MIN_L2.   [Dataset],   Aeris.
691   https://doi.org/10.25326/91, 2020.

692   16 Cermak, J. and Bendix, J.: Detecting ground fog from space - a microphysics-based approach, Int. J.
693   Remote Sens., 32, 3345-3371, https://doi.org/10.1080/01431161003747505, 2011.

694   17 Crewell. S., and Löhnert, U.: Accuracy of cloud liquid water path from ground-based microwave
695   radiometry 2. Sensor accuracy and synergy, Radio. Sci., 38(3), 8042,
696   https://doi.org/10.1029/2002RS002634, 2003.

697   18 Delanoë, J., Protat, A., Vinson, J.-P., Brett, W., Caudoux, C., Bertrand, F., Du Chatelet, J. P., Hallali,
698   R., Barthes, L., Haeffelin, M., et al.: BASTA: A 95-GHz FMCW Doppler Radar for Cloud and Fog
699   Studies, J. Atmos. Ocean. Technol. 33, 10231038: https://doi.org/10.1175/JTECH-D-15-0104.1,
700   2016.

701   19 Dhangar, N.G., Lal, D.M., Ghude, S.D. et al.: On the Conditions for Onset and Development of Fog
702   Over New Delhi: An Observational Study from the WiFEX, *Pure Appl. Geophys.* 178, 3727-3746,
703   https://doi.org/10.1007/s00024-021-02800-4, 2021.

704   20 Dias Neto, J., Nuijens, L., Unal, C., and Knoop, S.: Combined wind lidar and cloud radar for high-
705   resolution wind profiling, Earth Syst. Sci. Data, 15, 769-789, https://doi.org/10.5194/essd-15-769-
706   2023, 2023.

707   21 Ducongé, L., C. Lac, B. Vié, T. Bergot, and J. D., Price, Fog in heterogeneous environments : The
708   relative importance of local and non-local processes on radiative-advective fog formation, *Q. J. R.*
709   *Meteor. Soc.*, *146*, 2522-2546, https://doi.org/10.1002/qj.3783, 2020.

710 22 Dupont, J.-C., Haeffelin, M., Protat, A., Bouniol, D., Boyouk, N., and Morille, Y.: Stratus-fog
711   formation and dissipation: a 6-day case study, Bound.-Layer. Meteorol., 143, 207-225,
712   https://doi.org/10.1007/s10546-012-9699-4, 2012.

713 23 Fathalli, M., Lac, C., Burnet, F., Vié B.: Formation of fog due to stratus lowering: An observational
714   and modeling case study, Q. J. R. Meteor. Soc., https://doi.org/10.1002/qj.4304, 2022.

715 24 Fernando, H. J., Gultepe, I., Dorman, C., Pardyjak, E., Wang, Q., Hoch, S. W., et al.: C-FOG: life of
716   coastal fog, Bull Am Meteor Soc 102(2):E244–E272. https://doi.org/10.1175/BAMS-D-19-0070.1,
717   2021.

718 25 Foken, T., Göckede, M., Mauder, M., Mahrt, L., Amiro, B. D., and Munger, J. W.: Post-field data
719   quality control, in: Handbook of Micrometeorology: A Guide for Surface Flux Measurement and
720   Analysis, edited by: Lee, X., Massman, W. J., and Law, B., Kluwer, Dordrecht, 181-208,
721   https://doi.org/10.1007/1-4020-2265-4, 2004.

722 26 Ghude, S. D., et al.: WiFEX: Walk into the warm fog over Indo Gangetic Plain region. Bulletin of
723   the American Meteorological Society., https://doi.org/10.1175/BAMS-D-21-0197.1, 2023.

724 27 Huang, H. B., Chen, C. Y.: Climatological aspects of dense fog at Urumqi Diwopu International
725   Airport and its impacts on flight on-time performance. Nat Hazards 81(2):1091-1106,
726   https://doi.org/10.1007/s11069-015-2121-z, 2016.

727 28 Haeffelin, M., Bergot, T., Elias, T., Tardif, R., Carrer, D., Chazette, P., Colomb, M., Drobinski, P.,
728   Dupont, E., Dupont, J.-C., Gomes, L., Musson-Genon, L., Pietras, C., Plana-Fattori, A., Protat, A.,
729   Rangognio, J., Raut, J.-C., Rmy, S., Richard, D., Sciare, J. and Zhang, X.: Parisfog: shedding new
730   light on fog physical processes. Bulletin of the American Meteorological Society., 91(6), 767-783,
731   https://doi.org/10.1175/2009BAMS2671.1, 2010.

732 29 Koračin, D., Dorman, C. E., Lewis, J. M., Hudson, J. G., Wilcox, E. M., Torregrosa A.: Marine fog:
733   a review, Atmos. Res., 143:142-175, https://doi.org/10.1016/j.atmosres.2013.12.012, 2014.

734 30 Kumer, V. M., Reuder, J., Dorninger, M., Zauner, R., Grubišić, V.: Turbulent kinetic energy
735   estimates from profiling wind LiDAR measurements and their potential for wind energy
736   applications, Renew Energy., 99, 898-910, https://doi.org/10.1016/j.renene.2016.07.014, 2016.

737 31 Liao, H., Jing, H., Ma, C., Tao, Q., Li, Z.: Field measurement study on turbulence field by wind
738   tower and Windcube Lidar in mountain valley, Journal of Wind Engineering and Industrial
739   Aerodynamics., 197, 104090, ISSN 0167-6105, https://doi.org/10.1016/j.jweia.2019.104090, 2020.

740 32 Liu, D. Y., Niu S. J., Yang, J., Zhao, L. J., Lü, J. J., Lu, C. S.: Summary of a 4-year fog field study in
741   northern Nanjing, Part 1: fog boundary layer, Pure. Appl. Geophys., 169(5-6), 809-819,
742   https://doi.org/10.1007/s00024-011-0343-x, 2012.

743 33 Liu, D. Y., Yan, W. L., Yang, J., Pu, M. J., Niu, S. J., Li, Z. H.: A study of the physical processes of
744   an advection fog boundary layer, Boundary- Layer. Meteor., 158, 125-138,
745   https://doi.org/10.1007/s10546-015-0076-y, 2016.

746   34 Maalick, Z., Kühn, T., Korhonen, H., Kokkola, H., Laaksonen, A. and Romakkaniemi, S.: Effect of
747   aerosol concentration and absorbing aerosol on the radiation fog life cycle, Atmospheric
748   Environment, 133, 26-33, https://doi.org/10.1016/j.atmosenv.2016.03.018, 2016.

749   35 Marke, T., Ebell, K., Löhnert, U., Turner, D. D.: Statistical retrieval of thin liquid cloud
750   microphysical properties using ground-based infrared and microwave observations, J. Geophys. Res.
751   Atmos., 121(24):14-558, https://doi.org/10.1002/2016JD025667, 2016.

752   36 Martinet, P., Unger, V., Burnet, F. *et al.:* A dataset of temperature, humidity, and liquid water path
753   retrievals from a network of ground-based microwave radiometers dedicated to fog investigation,
754   *Bull. of Atmos. Sci. Technol.,* **3**, 6, https://doi.org/10.1007/s42865-022-00049-w, 2022.

755   37 Martinet, P. (2021). SOFOG3D_CHARBONNIERE_CNRM_MWR-HATPRO-LWP_L2. [Dataset].
756   Aeris. https://doi.org/10.25326/207

757   38 Mauder, M., Cuntz, M., Drüe, C., Graf, A., Rebmann, C., Schmid, H. P., Schmidt, M., and
758   Steinbrecher, R.: A strategy for quality and uncertainty assessment of long-term eddy-covariance
759   measurements,   Agr.   Forest   Meteorol.,   169,   122-135,
760   https://doi.org/10.1016/j.agrformet.2012.09.006, 2013.

761   39 Mazoyer, M., Lac, C., Thouron, O., Bergot, T., Masson, V., and Musson-Genon, L.: Large eddy
762   simulation of radiation fog: impact of dynamics on the fog life cycle, *Atmos. Chem. Phys.*, *17*,
763   13017-13035, https://doi.org/10.5194/acp-17-13017-2017, 2017.

764   40 Nakanishi M.: Large-Eddy simulation of radiation fog, Bound-Layer Meteor., 94, 461-493,
765   https://doi.org/10.1023/A:1002490423389, 2000.

766   41 Niu, S., Lu , C., Yu , H., Zhao, L., and Lü, L.: Fog research in China: an overview, Adv. Atmos.
767   Sci., 27(3), 639-662, https://doi.org/10.1007/s00376-009-8174-8, 2010a.

768   42 Niu, S., Lu , C., Zhao , J., Lu, J, and Yang , J.: Analysis of the microphysical structure of heavy fog
769   using a droplet spectrometer: a case study, Adv. Atmos. Sci., 27(6), 1259-1275,
770   https://doi.org/10.1007/s00376-010-8192-6, 2010b.

771   43 Pauli, E., Cermak, J., Andersen, H.: A satellite-based climatology of fog and low stratus formation
772   and dissipation times in central Europe, Q. J. Roy. Meteorol. Soc., 148, 1439-1454,
773   https://doi.org/10.1002/qj.4272, 2022.

774   44 Philip, A., Bergot, T., Bouteloup, Y., and Bouyssel, F.: The impact of vertical resolution on fog
775   forecasting in the kilometric-scale model Arome: a case study and statistics, Weather Forecast., 31,
776   1655-1671, https://doi.org/10.1175/WAF-D-16-0074.1, 2016.

777   45 Pithani, P., Ghude, S.D., Jenamani, RK., Biswas, M., Naidu, C.V., Debnath, S., Kulkarni, R.,
778   Dhangar, N.G., Jena, C., Hazra, A., Phani, R., Mukhopadhyay, P., Prabhakaran, T., Nanjundiah,
779   R.S., Rajeevan, M.: Real-time Forecast Of Dense Fog Events Over Delhi: The Performance Of the
780   WRF Model During WiFEX Field Campaign. Weather and Forecasting, 35(2), 739-756,
781   https://doi.org/10.1175/waf-d-19-0104.1, 2020.

782   46 Price, J. D.: On the formation and development of radiation fog: an observational study. Bound-
783   Layer Meteor., 172, 167-197, https://doi.org/10.1007/s10546-019-00444-5, 2019.

784   47 Price, J. D., Lane, S., Boutle, I. A., Smith, D. K. E., Bergot, T., Lac, C., Duconge, L., McGregor, J.,
785   Kerr-Munslow, A., Pickering, M., and Clark, R.: LANFEX: a field and modeling study to improve
786   our understanding and forecasting of radiation fog, *Bull. Amer. Meteo. Soc.*, *99*, 2061-2077,
787   https://doi.org/10.1175/BAMS-D-16-0299.1, 2018.

788   48 Price, J.: Radiation Fog. Part I: Observations of Stability and Drop Size Distributions, Boundary-
789   Layer Meteorol., 139, 167-191, https://doi.org/10.1007/s10546-010-9580-2, 2011.

790   49 Price, J., Porson, A., and Lock, A.: An observational case study of persistent fog and comparison
791   with an ensemble forecast model, Boundary-Layer. Meteorol., 155, 301-327,
792   https://doi.org/10.1007/s10546-014-9995-2, 2015.

793   50 Roach, W.: Back to basics: Fog: Part 2 - the formation and dissipation of land fog, Weather., 50(1),
794   7-11, 1995.

795   51 Román-Cascón, C., Steeneveld, G. J., Yagüe, C., Sastre, M., Arrillaga, J. A., and Maqueda, G.:
796   Forecasting radiation fog at climatologically contrasting sites: Evaluation of statistical methods and
797   WRF. Q. J. R. Meteorol. Soc., 142(695), 1048-1063, https://doi.org/10.1002/qj.2708, 2016.

798   52 Ryznar, E.: Advection-radiation fog near Lake Michigan, Atmos. Environ. 11, 427-430,
799   https://doi.org/10.1016/0004-6981(77)90004-X, 1977.

800   53 Steeneveld, G. J., Ronda, R. J., and Holtslag, A. A. M.: The challenge of forecasting the onset and
801   development of radiation fog using mesoscale atmospheric models, Boundary-Layer Meteorology,
802   154(2), 265-289, https://doi.org/10.1007/s10546-014-9973-8, 2015.

803   54 Tardif, R. and Rasmussen, R. M.: Event-based climatology and typology of fog in the New York
804   City region, J. Appl. Meteorol. Clim., 46, 1141-1168, https://doi.org/10.1175/JAM2516.1, 2007.

805   55 Ju, T., Wu, B., Zhang, H., Liu, J., 2020.: Characteristics of turbulence and dissipation mechanism in
806   a polluted advection-radiation fog life cycle in Tianjin, Meteorology and Atmospheric Physics.,
807   https://doi.org/10.1007/s00703-020-00764-z, 2020.

808   56 Toledo, F., Haeffelin, M., Wærsted, E., and Dupont, J.-C.: A new conceptual model for adiabatic
809   fog, Atmos. Chem. Phys., 21, 13099–13117, https://doi.org/10.5194/acp-21-13099-2021, 2021.

810   57 Felipe Toledo Bittner. Improvement of cloud radar products for fog surveillance networks : fog life
811   cycle analyses and calibration methodologies, Ph.D. Thesis, Institut Polytechnique de Paris, France,
812   ⟨NNT : 2021IPPAX029⟩. ⟨tel-03298445⟩, 2021.

813   58 Toledo, F., Delanoë, J., Haeffelin, M., Dupont, J.-C., Jorquera, S., and Le Gac, C.: Absolute
814   calibration method for frequency-modulated continuous wave (FMCW) cloud radars based on corner
815   reflectors, Atmos. Meas. Tech., 13, 6853-6875, https://doi.org/10.5194/amt-13-6853-2020, 2020.

816 59 Wærsted, E. G., Haeffelin, M., Steeneveld, G.-J., and Dupont, J.-C.: Understanding the dissipation of
817   continental fog by analysing the LWP budget using idealized LES and in situ observations, Q. J.
818   Roy. Meteor. Soc., 145, 784-804, https://doi.org/10.1002/qj.3465, 2019.

819 60 Wærsted, E. G. Description of physical processes driving the life cycle of radiation fog and fog-
820   stratus transitions based on conceptual models, Ph.D. Thesis, Paris Saclay, 2018.

821 61 Wærsted, E. G., Haeffelin, M., Dupont, J.-C., Delanoë, J., and Dubuisson, P.: Radiation in fog:
822   quantification of the impact on fog liquid water based on ground-based remote sensing, Atmos.
823   Chem. Phys., 17, 10811–10835, https://doi.org/10.5194/acp-17-10811-2017, 2017.

824 62 Walker, M.: The science of weather: Radiation fog and steam fog, Weather, 58, 196-197,
825   https://doi.org/10.1256/wea.49.02, 2003.

826 63 Zhou, B., and Ferrier, B. S.: Asymptotic analysis of equilibrium in radiation fog. Journal of Applied
827   Meteorology and Climatology, 47, 1704-1722. https://doi.org/10.1175/2007JAMC1685.1, 2008.

List of tables

Table 1 : Case study number, fog onsets, type of fog formation, fog dissipation times, fog duration and type of fog dissipation for the four documented case studies. Time is in UTC. Dates are in the format "dd/mm/yyyy". "dd" indicates the day, "mm" the month, and "yyyy" the year.

Table 2 : Summary of fog features at the supersite during the five defined phases during its evolution for each case study. The formation, dissipation times are estimated using the visibility (m) from the Scatterometer. The transition from stable to adiabatic fog is defined using temperature from the microwave radiometer. The cooling rate (dT/dt), wind speed (WS), and wind direction (WD) are derived from the meteorological station. Sensible heat flux (SHF), turbulent kinetic energy (TKE) and the vertical velocity variance (σ_w^2) at 3 m a.g.l are derived from the flux station. The liquid water path (LWP) is estimated from the MWR. The fog reservoir of liquid weather path (RLWP) and the equivalent adiabaticity of closure $\alpha_{eq}^{closure}$ parameter are computed by the conceptual model. Cloud top height (CTH) and middle and high cloud base and top heights are derived from the radar reflectivity from Basta cloud radar."-" indicates that the variables are not measurable or calculable.

height (ITH) (open gray circles), inversion base height (IBH) (open gray squares), cloud top height (CTH) from the cloud radar (open black squares), and the cloud base height (CBH) from the Ceilometer (open black circles). In (d) wind speed (shaded) and direction (arrows) from the WindCube. Arrows in (d) indicate only the direction of the horizontal flow. Time evolution of (e) air temperature at 3 m a.g.l from the meteorological station (red line) and equivalent adiabaticity of closure from the fog conceptual model (blue line), (f) the mean of the turbulent kinetic energy (TKE) in the layer 40 – 220 m for the WindCube (black line) and the TKE (blue line) and vertical velocity variance (red line) at 3 m a.g.l from the flux station at Charbonnière, (g) the LWP estimate from the MWR (blue line), the RLWP from the fog conceptual model (red line), and (h) sensible heat fluxes (SHF) (red and blue lines, respectively) from the flux station. Vertical black dashed lines indicate fog formation and dissipation times. Green dashed lines indicate the transition period (fog mature phase) from stable to adiabatic fog. The red dashed line indicates sunrise.

Figure 5: As in Figure 3 but for the 5-6 January 2020 (case study 2, IOP 6). In (c), only Charbonnière and Noaillan have valid data. In (c), the visibility measured at Moustey, Tuzan and Cape Sud were interrupted by technical issues.

Figure 6: As in Figure 4 but for the 5-6 January 2020 (case study 2, IOP6).

Figure 7: As in Figure 3 but for the 8-9 February 2020 (case study 3, IOP 11).

Figure 8: As in Figure 4 but for the 8-9 February 2020 (case study 3, IOP 11).

Figure 9: As in Figure 3 but for the 7-8 March 2020 (case study 4, IOP 14).

Figure 10: As in Figure 4 but for the 7-8 March 2020 (case study 4, IOP 14). The LWP, RLWP, and $\alpha_{eq}^{closure}$ are disrupted between 00:30 and 02:30 UTC because the LWP estimated by the MWR take into account the liquid water in the advected stratus.

Figure 11: Vertical profiles of air temperature and radar reflectivity put together for each fog case study: (a) for case study 1, (b) case study 2, (c) case study 3 and (d) case study 4. Line and shaded area indicate the mean and standard deviation of air temperature and radar reflectivity during each fog phase.

900 ***Table 2 :*** *Summary of fog features at the supersite, during the five defined phases during it evolution for each case study.*
901 *The formation, dissipation times are estimated using the visibility (m) from Scatterometer. The cooling rate (dT/dt), wind*
902 *speed (WS) and wind direction (WD) are derived from the meteorological station. Sensible heat flux (SHF), turbulent*
903 *kinetic energy (TKE), and the vertical velocity variance (σ_w^2) at 3 m a.g.l are derived from the flux station. The liquid*
904 *water path (LWP) is estimated from the MWR. The fog reservoir of liquid weather path (RLWP) and the equivalent*
905 *adiabaticity of closure $\alpha_{eq}^{closure}$ parameter are computed by the conceptual model. Cloud top height (CTH) and middle*
906 *and high cloud base and top heights are derived from the radar reflectivity from Basta cloud radar."-" indicates that the*
907 *variables are not measurable or calculable.*

Case study number	Phase names	Time range (UTC)	Duration (h:min)	Visibility (m)	dT/dt (°C h⁻¹)	$\alpha_{eq}^{closure}$ (g m⁻³)	LWP (g m⁻²)	RLWP max (g m⁻²)	CTH (m a.g.l)	WS (m s⁻¹)	WD (°)	TKE (m² s⁻²)	σ_w^2 (m² s⁻²)	SHF (W m⁻²)	Cloud above fog (m a.g.l)
1 (IOP5)	Pre-fog	[20:50 - 22:50]	2:00	9962	-0.9	-	0	-	-	0.61	61	0.11	0.002	-0.23	clear
	Stable	[22:50 - 05:00]	6:10	736	-0.18	-1.3	2	-	50	0.7	84	0.07	0.01	-1.16	clear
	Transition stable/adiabatic	[05:00 - 07:00]	2:00	173 – 262	0.08	-0.8 – 0.4	7 – 28	8 – 15	75 – 187.5	0.5 – 2.1	68 – 112	0.06 – 0.15	0.02 – 0.03	2.3 – 8.8	clear
	Adiabatic	[07:00 - 11:00]	4:00	370	0.77	0.5	26	6	187.5	2.4	116	0.23	0.04	12.9	[8000 - 10000]
	Dissipation	[10:30 - 11:30]	1:00	1549	1.1	0.63	43	-11	287.5	2.6	94	0.36	0.06	22.02	clear
2 (IOP6)	Pre-fog	[18:40 - 20:40]	2:00	15566	-0.7	-	0	-	-	0.2	195	0.03	0.003	-0.17	clear
	Stable	[20:40 - 00:00]	3:20	242	-0.13	-0.69	2	-	75	1	183	0.06	0.009	0.28	clear
	Transition stable/adiabatic	[00:00 - 02:00]	2:00	219 – 291	-0.007	-0.2 – 0.45	1 – 17	-1 – 4	75 – 162.5	1.6 – 2.6	149 – 147	0.15 – 0.23	0.02 – 0.04	3.7 – 11	clear
	Adiabatic	[02:00 - 08:40]	6:40	450	0.17	0.51	22	1	187.5	2.2	110	0.21	0.04	6.62	clear
	Dissipation	[08:10 - 09:10]	1:00	944	0.43	0.53	12	-8	187.5	2.5	136	0.28	0.048	14.02	[250 - 1000]
3 (IOP11)	Pre-fog	[18:40 - 20:40]	2:00	13239	-1.03	-	0	-	-	1.3	242	0.05	0.011	-5.5	rain
	Stable	[20:40 - 23:00]	2:20	243	-1.2	-0.69	6	-	75	1	220	0.03	0.002	-1.7	clear
	Transition stable/adiabatic	[23:00 - 02:30]	3:30	134 – 260	-0.08	-1.35 – 0.4	5 – 20	8 – 6	50 – 150	1.8 – 0.4	144 – 78	0.06 – 0.03	0.006 – 0.004	-1.9 – -0.2	clear
	Adiabatic	[02:30 - 03:40]	1:10	271	0.81	0.54	31	3	200	1	120	0.04	0.008	-0.49	clear
	Dissipation	[03:10 - 04:10]	1:00	1445	1.34	0.6	42	2	237.5	3.6	143	0.33	0.07	-3.02	clear
4 (IOP14)	Pre-fog	[19:20 - 21:20]	2:00	14088	-0.47	-	0	-	-	1.1	233	0.02	0.002	-1.17	[5000 - 6000] [8000 - 10000]
	Stable	[21:20 - 23:30]	2:10	230	-0.88	-0.46	11	-	87.5	1.2	177	0.06	0.012	-3.26	clear
	Transition stable/adiabatic	[23:30 - 01:00]	1:30	240 – 253	0.12	-0.17 – 0.64	11 – 59	10 – -	100 – 200	1.6 – 2.7	141 – 184	0.06 – 0.27	0.01 – 0.05	-1.6 – 2.7	clear
	Adiabatic	[00:20 - 04:00]	3:40	372	0.47	0.59	43	8.10	287.5	2	179	0.17	0.03	1.2	[250 - 500]
	Dissipation	[03:30 - 04:30]	1:00	1160	-0.14	0.60	40	-2	237.5	2.7	174	0.23	0.04	0.82	clear

(a)   (b)
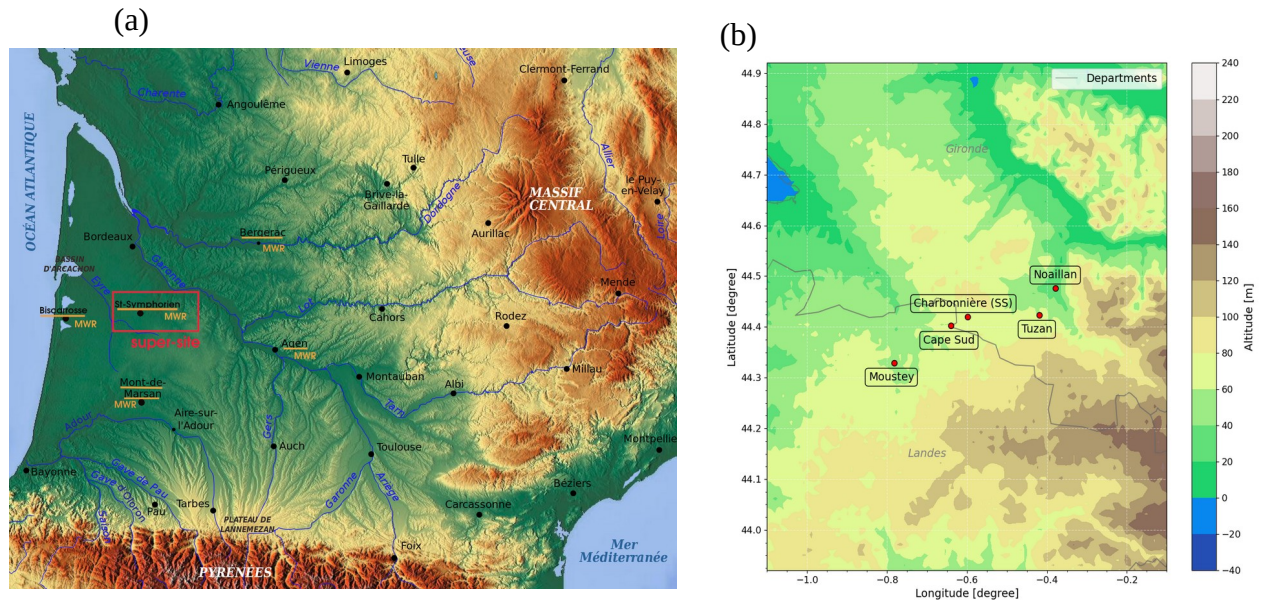
Figure 1 : In a), the orography of the study area of the SOFOG3D field campaign including the five instrumented sites (Agen, Bergerac, Biscarrosse, Mont-de-Marsan, and Saint-Symphorien) where a microwave radiometer was installed (adapted from https://fr.wikipedia.org/wiki/Grand_Sud-Ouest_fran%C3%A7ais#/media/Fichier:Topographic_map_of_South-West_France_with_main_rivers_and_cities.svg). Blue lines indicate the rivers. The cities are indicated in black dots. The most instrumented domain around the supersite is indicated in a) by the red rectangle. In b), the orography of a 100 x 100 km^2 domain centered on Charbonnière which includes locations of four of the meteorological stations installed around the supersite and used in this study. Orography data are from the National Aeronautics and Spatial Administration (NASA) shuttle radar topography mission (SRTM) (90 m of resolution).
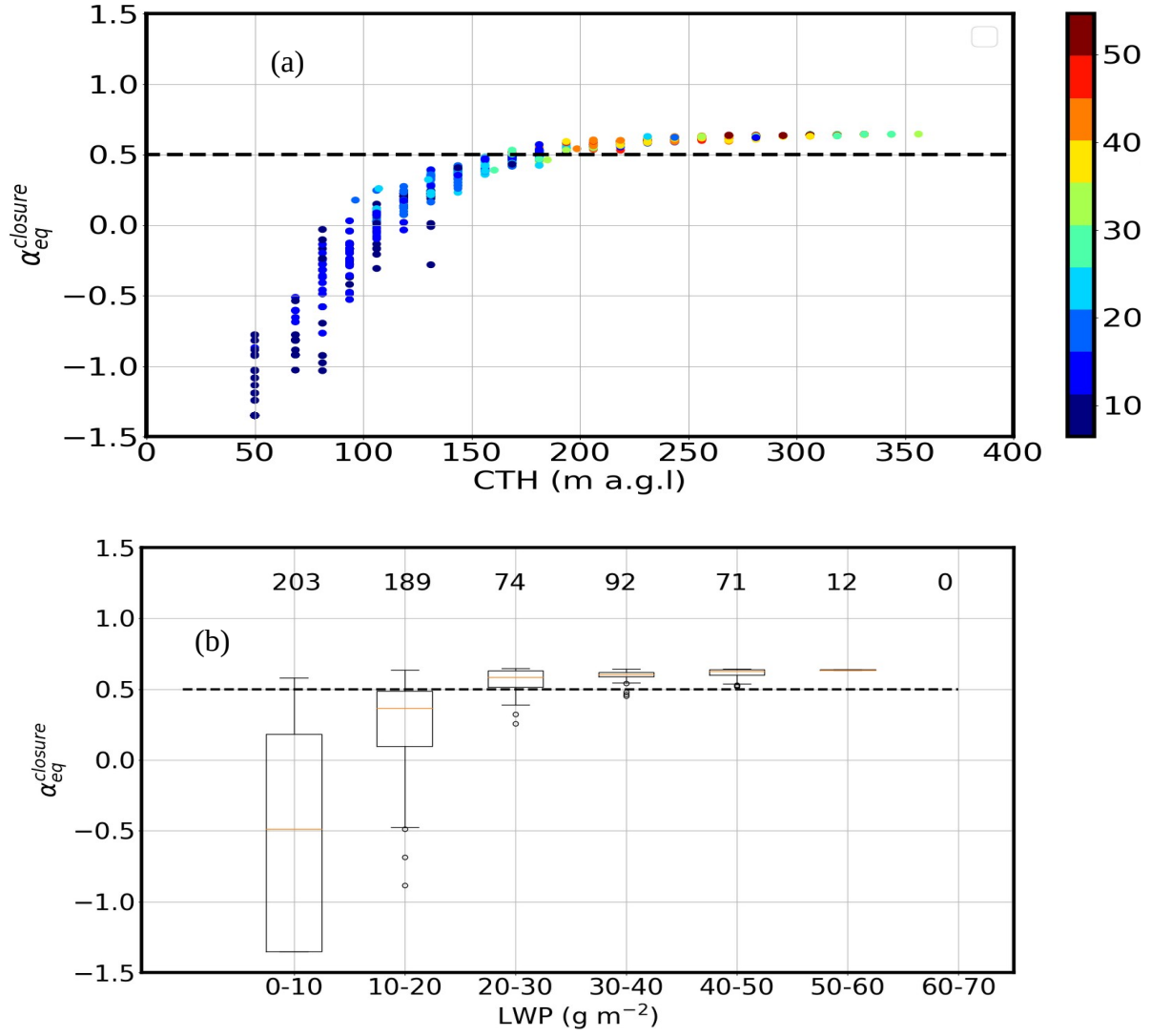
Figure 2: In (a) Scatter plot of the equivalent adiabaticity by closure versus the CTH and LWP (colored circles) at the supersite. b) Boxplot of the equivalent adiabaticity by closure versus the different LWP ranges from the MWR. In b), numbers at the figure top indicate total values included in each boxplot and computed between 2 hours before and after the fog. Horizontal dashed line indicates the threshold of the equivalent adiabaticity from closure defining the transition from stable to adiabatic fog.
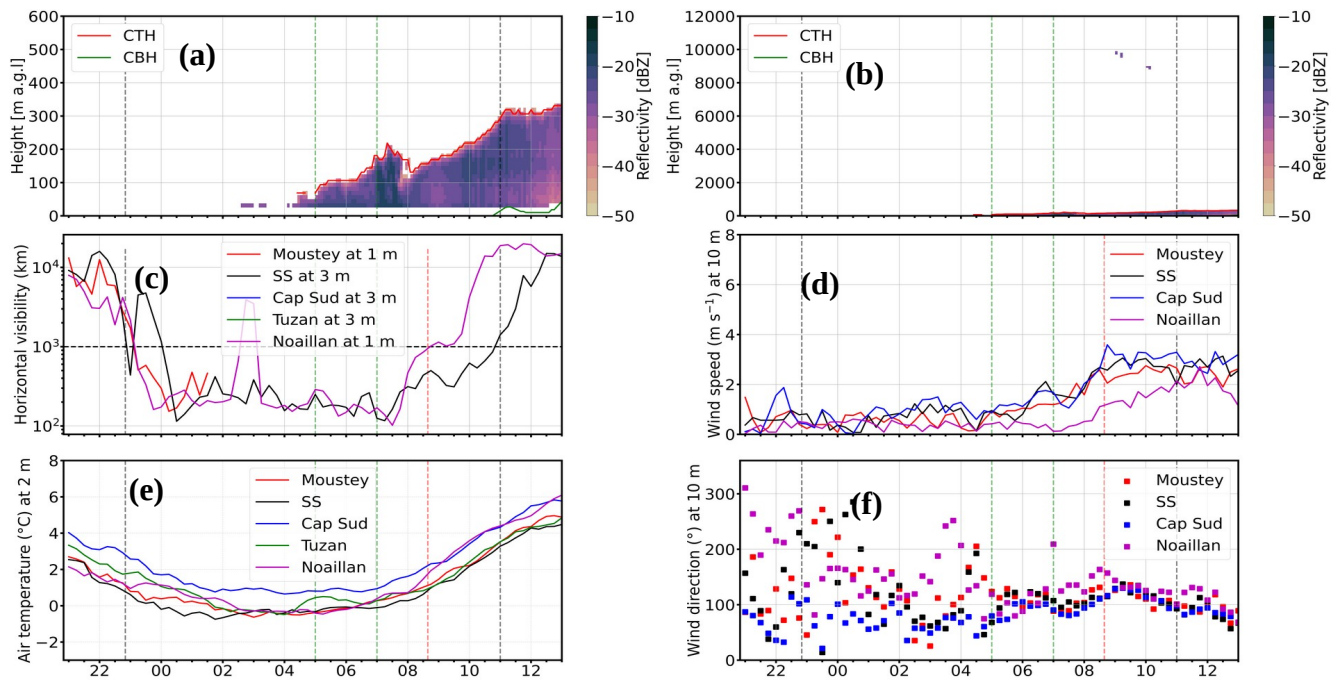
Figure 3: In (a-b) time-height cross-section from surface up to 600 and 12000 m, respectively of radar reflectivity from Basta (shaded) radar, time evolution of the cloud top height from Basta (red line), and the cloud base height from the Celiometer (CL51) (green line). Time evolution of (c) surface visibility, (d) 10 m wind speed, (e) 2 m air temperature, and (f) 10 m wind direction observed on the 28-29 December 2019 (case study 1, IOP 5) at the five meteorological stations (in red, black, blue, green, and pink lines for Moustey (1 m a.g.l), Charbonnière (3 m a.g.l), Cape Sud (3 m a.g.l), Tuzan (3 m a.g.l), and Noaillan (1 m a.g.l), respectively) deployed around the supersite. Note that wind was not collected at Tuzan. In (c), the visibility measured at Moustey was interrupted by technical issues. Vertical black dashed lines indicate fog formation (left) and dissipation (right) times. Green dashed lines show the transition time from stable fog to adiabatic fog (fog mature phase). Red dashed line indicates the sunrise.
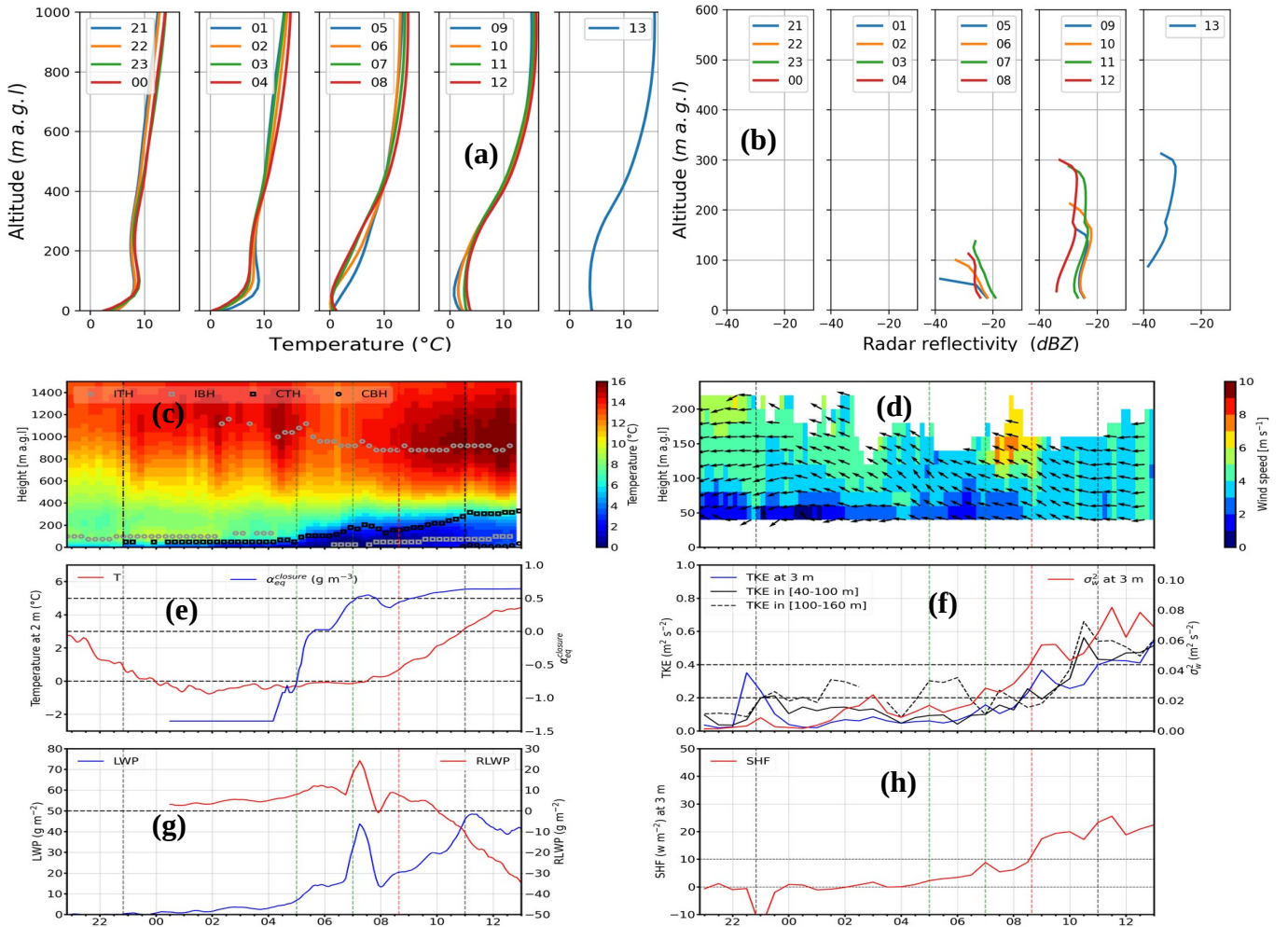
Figure 4: Evolution of fog macrophysical characteristics observed on the 28-29 December 2019 (case study 1, IOP 5) at Charbonnière. In (a-b) vertical profiles of air temperature from the Hatpro microwave radiometer (MWR) and radar reflectivity from Basta radar, respectively. In (c) time-height cross-section of air temperature from the MWR (shaded), time evolution of inversion top height (ITH) (open gray squares), inversion base height (IBH) (open gray squares), cloud top height (CTH) from the cloud radar (open black squares), and the cloud base height (CBH) from the Celiometer (open black circles). In (d) wind speed (shaded) and direction (arrows) from the WindCube. Arrows in (d) indicate only the direction of the horizontal flow. Time evolution of (e) air temperature at 3 m a.g.l from the meteorological station (red line) and equivalent adiabaticity of closure from the fog conceptual model (blue line), (f) the mean of the turbulent kinetic energy (TKE) in the layer 40 – 220 m for the WindCube (black line) and the TKE (blue line) and vertical velocity variance (red line) at 3 m a.g.l from the flux station at Charbonnière, (g) the LWP estimate from the MWR (blue line), the RLWP from the fog conceptual model (red line), and (h) sensible heat fluxes (SHF) (red and blue lines, respectively) from the flux station. Vertical black dashed lines indicate fog formation and dissipation times. Green dashed lines indicate the transition period (fog mature phase) from stable to adiabatic fog. The red dashed line indicates sunrise.

950 **Figure 5:** As in Figure 3 but for the 5-6 January 2020 (case study 2, IOP 6). In (c), only Charbonnière

951 and Noaillan have valid data. In (c), the visibility measured at Moustey, Tuzan and Cape Sud were

952 interrupted by technical issues.
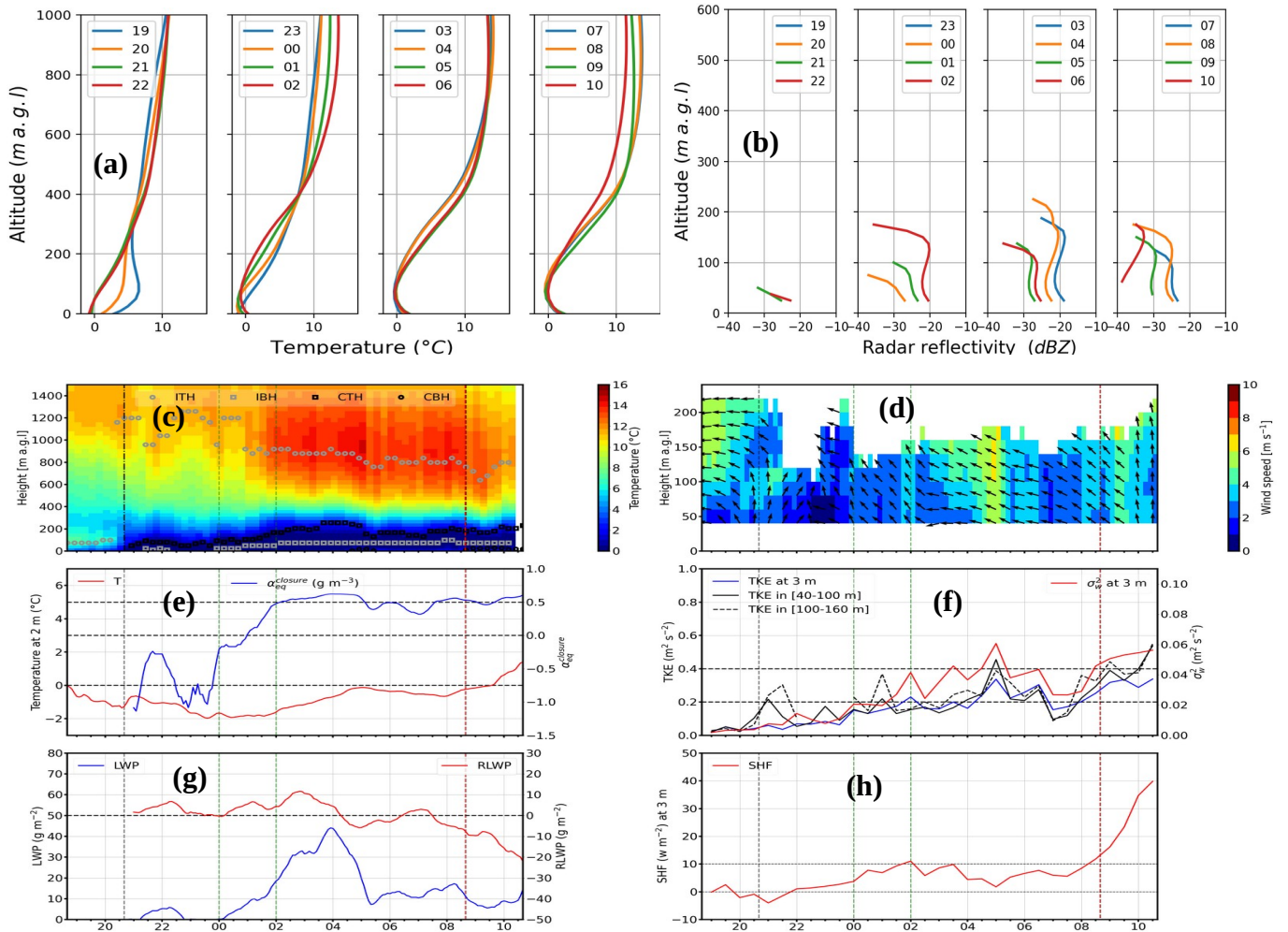
Figure 6: As in Figure 4 but for the 5-6 January 2020 (case study 2, IOP6). The red vertical dashed line indicates the sunrise.
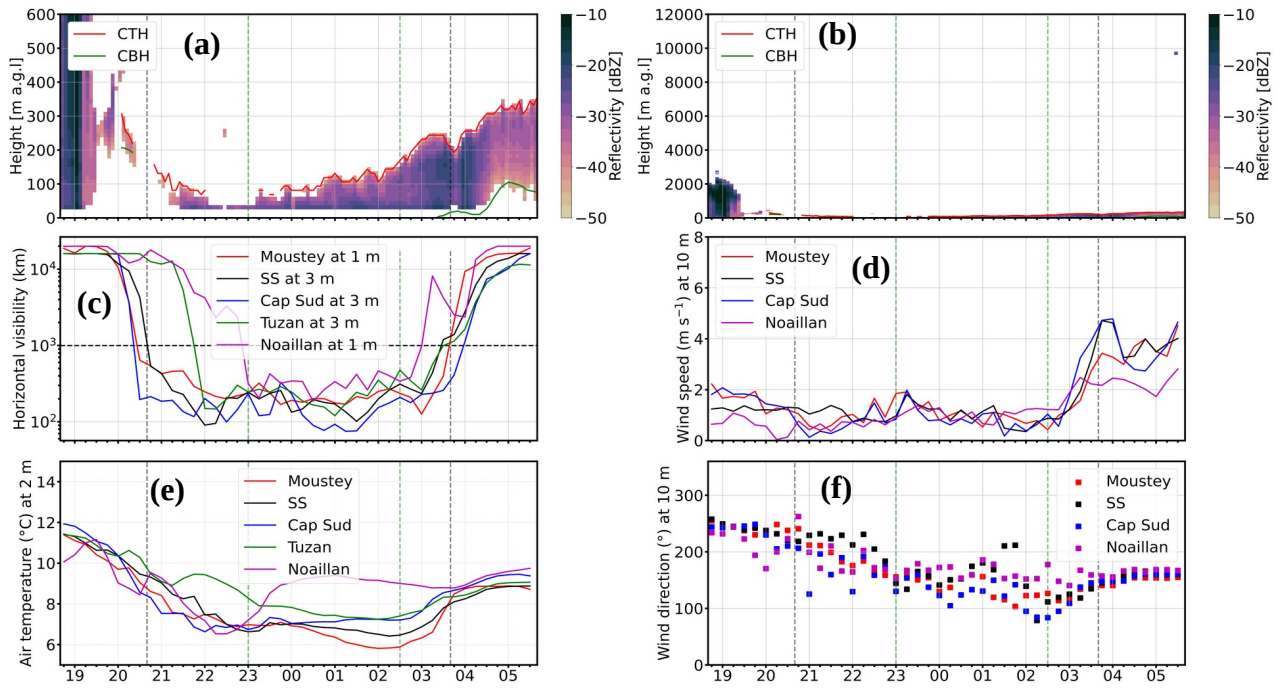
 Figure 7 : As in Figure 3 but for the 8-9 February 2020 (case study 3, IOP 11)
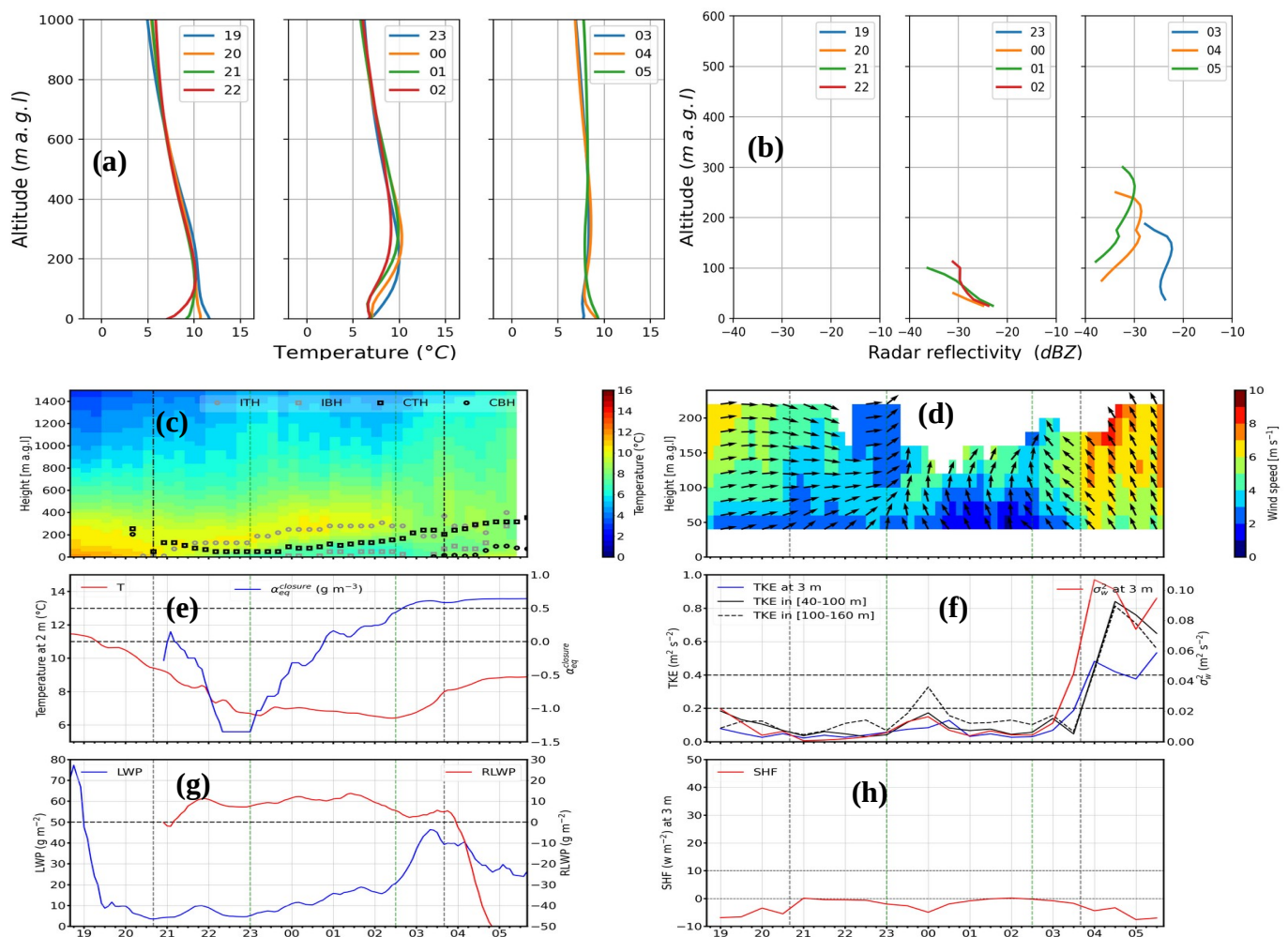
Figure 8: As in Figure 4 but for the 8-9 February 2020 (case study 3, IOP 11).
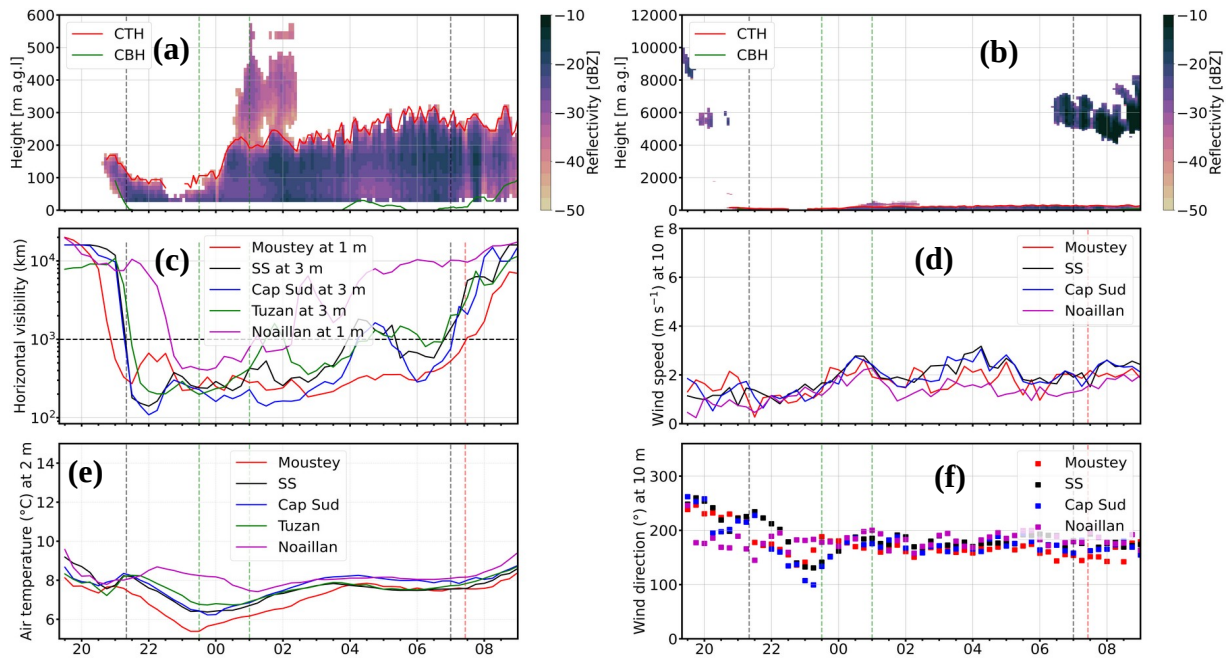
957 **Figure 9 :** As in Figure 3 but for the 7-8 March 2020 (case study 4, IOP 14).
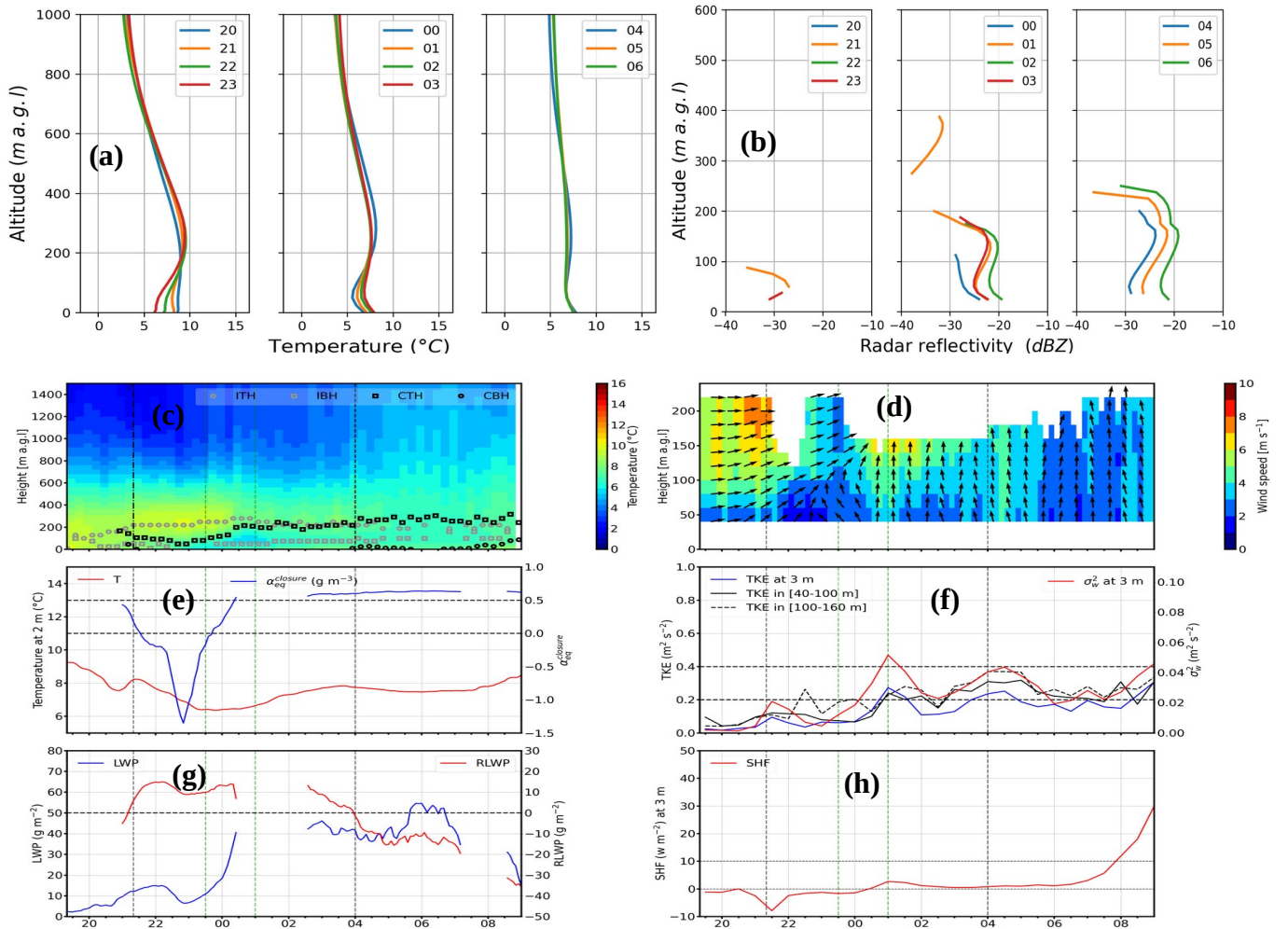
958 **Figure 10 :** As in Figure 4 but for the 7-8 March 2020 (case study 4, IOP 14). The LWP, RLWP, and

959 $\alpha_{eq}^{closure}$ are disrupted between 00:30 and 02:30 UTC because the LWP estimated by the MWR take

960 into account the liquid water in the advected stratus.
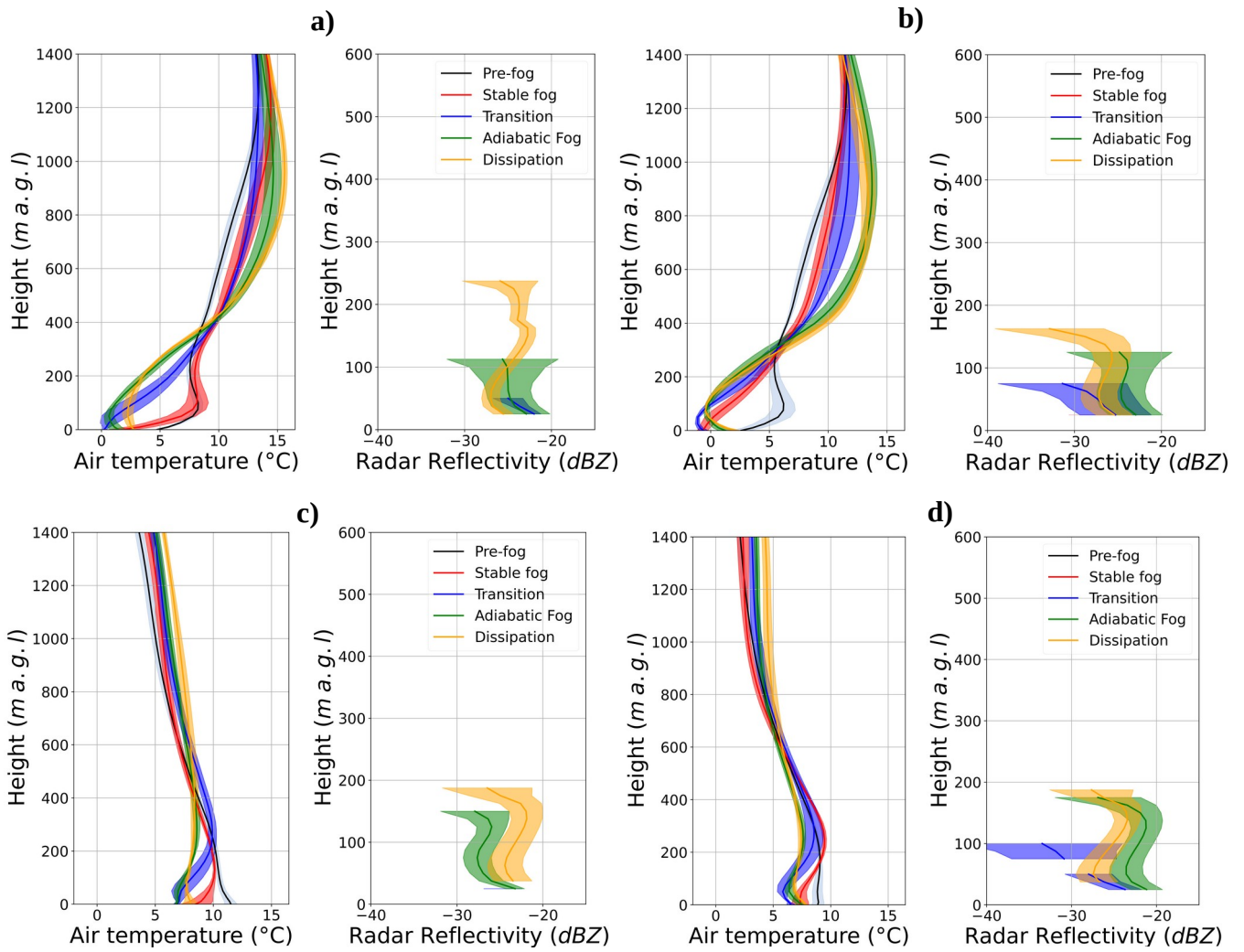
961 **Figure 11:** Vertical profiles of air temperature and radar reflectivity put together for each fog case study (a) for case 1,

962 (b) case 2, (c) case 3 and (d) case 4. Line and shaded area indicate the mean and standard deviation of air temperature

963 and radar reflectivity during each fog phase.